



저작자표시-비영리-변경금지 2.0 대한민국

이용자는 아래의 조건을 따르는 경우에 한하여 자유롭게

- 이 저작물을 복제, 배포, 전송, 전시, 공연 및 방송할 수 있습니다.

다음과 같은 조건을 따라야 합니다:



저작자표시. 귀하는 원 저작자를 표시하여야 합니다.



비영리. 귀하는 이 저작물을 영리 목적으로 이용할 수 없습니다.



변경금지. 귀하는 이 저작물을 개작, 변형 또는 가공할 수 없습니다.

- 귀하는, 이 저작물의 재이용이나 배포의 경우, 이 저작물에 적용된 이용허락조건을 명확하게 나타내어야 합니다.
- 저작권자로부터 별도의 허가를 받으면 이러한 조건들은 적용되지 않습니다.

저작권법에 따른 이용자의 권리와 책임은 위의 내용에 의하여 영향을 받지 않습니다.

이것은 [이용허락규약\(Legal Code\)](#)을 이해하기 쉽게 요약한 것입니다.

[Disclaimer](#)



이학박사 학위논문

**Investigation of spatial transcriptomic
signatures and therapeutic mode of action
in Alzheimer's disease mouse model**

알츠하이머병 모델에서 공간 전사체 시그니처
및 치료 작용 원리 규명

2022년 8월

서울대학교 융합과학기술대학원

분자의학 및 바이오제약학과

이 은 지

Investigation of spatial transcriptomic signatures and therapeutic mode of action in Alzheimer's disease mouse model

알츠하이머병 모델에서 공간 전사체 시그니처
및 치료 작용 원리 규명

지도교수 이 동 수

이 논문을 이 은 지 박사 학위논문으로 제출함

2022년 04월

서울대학교 융합과학기술대학원
분자의학 및 바이오제약학과
이 은 지

이 은 지의 이학박사 학위논문을 인준함

2022년 06월

| | |
|-------|------------------|
| 위 원 장 | <u>이 유 진 (인)</u> |
| 부위원장 | <u>이 동 수 (인)</u> |
| 위 원 | <u>신 영 기 (인)</u> |
| 위 원 | <u>최 홍 윤 (인)</u> |
| 위 원 | <u>황 도 원 (인)</u> |

ABSTRACT

Investigation of spatial transcriptomic signatures and therapeutic mode of action in Alzheimer's disease mouse model

Eun Ji Lee

Department of Molecular Medicine and Biopharmaceutical Science,
The Graduate School of Convergence Science and Technology,
Seoul National University

Although the pathophysiological changes that occur with the progression of Alzheimer's disease (AD) are well-known, understanding the overall spatial heterogeneity of the brain is still required. Furthermore, there are insufficient methods to comprehensively verify the therapeutic effect in AD, a multifactorial disease. Advances in technology allow the use of spatial transcriptome data to identify key gene signatures and associated biological pathways in individual brain regions. In this study, I established a workflow to extensively perform each brain region-based spatial transcriptomic analysis to

study the pathological changes in AD and evaluate the therapeutic action of immunomodulators that exhibit behavioral-improving effects.

First, I applied the workflow to compare AD model of different ages before and after definite accumulation of amyloid plaques. Early alterations of the AD model were identified exclusively in the white matter and were primarily involved in glial cell activation. In the later stage of AD, genes associated with glial cell activation were globally upregulated in both the white and gray matter, whereas the downregulated genes were region-specific. I also investigated spatial patterns of major brain cells using a curated reference-based marker panel. I identified the initial changes in the microglia and astrocytes-related signatures in the white matter, which eventually spread to the gray matter. Additionally, I observed various alterations in each brain regions, including genes involved in the diverse neuronal subclasses, metabolic process, and senescence, with the progression of AD pathology.

I evaluated the therapeutic effect of natural killer (NK) cell supplements and anti-CD4 antibody (aCD4), which improved behavior function identified via a Y-maze behavioral test in the AD model. NK cell therapy showed a decrease in glial cell-related genes and an increase in cellular respiration-related genes throughout the brain regions. Among the glial cell signatures, the decrease in the expression of activated microglial signatures was remarkable. The alteration was prominent in the cortex and thalamus but also occurred throughout the region. Moreover, a decrease in the inhibitory neuronal signatures in the amygdala was observed after NK cell administration in the AD model. In contrast, aCD4-injected AD model revealed region-specific

changes exclusively in the white matter. Although not dramatic, synaptic function-related genes showed an increased expression level in the white matter. The changes in major brain cell signatures were insignificant after aCD4 administration in the AD model.

These results help to understand the spatiotemporal changes associated with the pathological progression of AD at a molecular level. Aberrantly altered major brain cell signatures were verified in each brain region of the AD model. Moreover, I demonstrated the feasibility of spatial transcriptome analysis as a method to validate the effects and modes of action in the AD model, taking two different drug administrations as examples. This workflow based on spatial transcriptomics can be harnessed to validate the therapeutic efficacy and mode of action via an in-depth transcriptional analysis in various diseases.

Keywords: Spatial transcriptomics; Spatial heterogeneity of brain; Alzheimer's disease; Brain cell signatures; Immunomodulatory drugs; NK cells; CD4 T cells

Student Number: 2018-35220

CONTENTS

| | |
|--|-------------|
| ABSTRACT | i |
| CONTENTS | iv |
| List of Figures | viii |
| List of Tables | x |
| 1. Introduction | 1 |
| 1.1 Spatially resolved transcriptomics | 1 |
| 1.2 Alzheimer's disease | 4 |
| 1.3 Pathological change of glial cells in AD | 6 |
| 1.4 AD therapeutics | 8 |
| 1.5 Final goal of the study | 9 |
| 2. Methods | 11 |
| 2.1 Experimental models | 11 |
| 2.1.1 AD models in different ages | 11 |
| 2.1.2 Peripheral CD4 T cell blockade in AD model | 11 |
| 2.1.3 NK cell supplement in AD model | 11 |
| 2.2 Data Analysis | 12 |
| 2.2.1 Spatial gene expression library construction | 12 |
| 2.2.2 Generation of count matrix | 13 |
| 2.2.3 Spatial transcriptome data: Integration and spot clustering..... | 13 |
| 2.2.4 Differential gene expression analysis | 14 |
| 2.2.5 Gene ontology analysis | 15 |
| 2.2.6 Marker panel selection and curation | 15 |
| 2.2.7 Cellular signatures of reference data | 15 |

| | |
|---|-----------|
| 2.2.8 Spot-based correlation analysis | 16 |
| 2.2.9 Statistical analysis | 16 |
| 2.3 Validation | 16 |
| 2.3.1 Immunofluorescence imaging for tissue sections | 16 |
| 2.3.2 Behavior analysis, Y-maze | 17 |
| 2.3.3 NK cell isolation and culture | 17 |
| 2.3.4 Flow cytometry for NK cell characterization | 17 |
| 2.3.5 IFN-gamma release assay by ELISA | 18 |
| 2.3.6 Isolation of samples and live cell dissociation | 18 |
| 2.3.7 MACS sorting of brain cells | 19 |
| 2.3.8 Flow cytometry for T cell population identification | 20 |
| 2.3.9 Statistical analysis | 20 |
| 3. Results | 21 |
| 3.1 Age-dependent change in the 5XFAD AD model | 21 |
| 3.1.1 Analytical workflow for spatial transcriptome data | 21 |
| 3.1.2 Identifying clusters corresponding to anatomical structures of the brain | 24 |
| 3.1.3 Investigation of DEGs in the AD model of different ages | 28 |
| 3.1.3.1 DEGs and related biological pathways in three-month-old AD model | 30 |
| 3.1.3.2 DEGs and related biological pathways in 7.5-month-old AD model | 31 |
| 3.1.3.3 Changes by brain regions according to the progression of amyloid pathology in AD model | 36 |

| | |
|---|------|
| 3.1.4 Spatial distribution of diverse cell signatures in the AD model.... | 41 |
| 3.1.4.1 Spatial distribution of the subtypes of glial cell signatures in AD model | 45 |
| 3.1.4.2 Spatial distribution of myeloid and lymphoid cell signatures in AD model | 51 |
| 3.1.4.3 Spatial distribution of the subclasses of neuronal signatures in AD model | 55 |
| 3.1.5 Spatial distribution of brain cell state-related signatures in the AD model | 59 |
| 3.1.5.1 Metabolism and senescence-related signatures | 59 |
| 3.2 Effect of NK cell supplement administration in the 5XFAD AD model | 63 |
| 3.2.1 Improvement of behavior function identified via the Y-maze in AD model after administration of NK cell supplements | 63 |
| 3.2.2 Characterization of isolated mouse splenic NK cells | 65 |
| 3.2.3 DEGs and related biological pathways after NK cell treatment in the AD model | 68 |
| 3.2.4 Biological pathways showing changes after NK cell treatment in AD model | 73 |
| 3.2.5 Changed spatial distribution of major brain cells after NK cell treatment in AD model | 76 |
| 3.2.6 <i>In vivo</i> SPECT/CT images and biodistribution of ^{99m}Tc -HMPAO- NK cells | ,,81 |
| 3.3 Effect of anti-CD4 antibody administration in the 5XFAD AD model .. | 84 |

| | |
|---|------------|
| 3.3.1 Improvement of behavior function identified via the Y-maze in the AD model injected with anti-CD4 antibody | 84 |
| 3.3.2 Changes in each brain region after anti-CD4 antibody treatment in AD model | 90 |
| 3.3.3 Changed spatial distribution of brain cell signatures after anti- CD4 antibody administration in AD model | 94 |
| 4. Discussion | 98 |
| 5. Conclusion | 109 |
| 6. Reference | 110 |
| ABSTRACT in Korean | 117 |

List of Figures

| | |
|--|----|
| Figure 1. Schematic workflow to identify differences between groups using spatial transcriptome data | 23 |
| Figure 2. Spatial transcriptome-based cluster analysis in three month- and 7.5 month-WT and AD model | 26 |
| Figure 3. Distinctive expression pattern in three- and 7.5-month-old WT and AD model | 29 |
| Figure 4. Identification of DEGs and related biological pathways in the AD model at three and 7.5 months compared to WT mice | 34 |
| Figure 5. Regional changes in the WT and TG mice from three months to 7.5 months | 38 |
| Figure 6. Identification of spatial changes in the distribution of diverse brain cells in 7.5-month-old WT and AD model | 46 |
| Figure 7. Spatial changes in the distribution of glial cell subtypes in AD models at different ages | 49 |
| Figure 8. Spatial changes in the distribution of myeloid and lymphoid cells in AD models at different ages | 53 |
| Figure 9. Identification of spatial changes in the distribution of neuronal subclasses in the AD models at different ages | 57 |
| Figure 10. Spatial patterns of metabolism- and senescence-related signatures in the WT and AD model at different ages | 61 |
| Figure 11. Improved behavior function after NK cell treatment in AD model | 64 |
| Figure 12. Characterization of isolated mouse splenic NK cells | 66 |

| | |
|--|----|
| Figure 13. Identification of DEGs and related biological pathways in the NK cell-treated compared to the saline-treated AD model | 70 |
| Figure 14. Upregulated and downregulated biological pathways in NK cell-treated AD model | 75 |
| Figure 15. Changes in brain cell signatures after NK cell treatment in AD model | 79 |
| Figure 16. <i>In vivo</i> SPECT/CT images and biodistribution of ^{99m}Tc -HMPAO-NK cells | 82 |
| Figure 17. Improved behavior function after anti-CD4 antibody treatment in AD model | 86 |
| Figure 18. Inactivation of peripheral CD4 T cells in the AD model after anti-CD4 antibody treatment | 88 |
| Figure 19. Changes in the white matter of AD model after the administration of anti-CD4 antibody | 92 |
| Figure 20. Changes in brain cell signatures after anti-CD4 antibody treatment in AD model | 96 |

List of Tables

| | |
|--|----|
| Table 1. Representative genes and associated biological pathways that change regionally in 7.5- compared to three-month-old WT mice | 40 |
| Table 2. Representative genes and associated biological pathways that change regionally in the 7.5- compared to three-month-old AD model, excluding the age-dependent changes in WT mice | 40 |
| Table 3. Summary of the spatiotemporal changes in the progression of amyloid pathology | 62 |
| Table 4. Representative genes and associated biological pathways that change regionally in NK cell-injected AD model, excluding the changes that occur in WT mice | 72 |
| Table 5. Representative genes and associated biological pathways that change regionally in anti-CD4 antibody injected AD model, excluding the changes that occur in WT mice | 93 |
| Table 6. Summary of the feasibility test of ST analysis for verifying the mode of action of AD therapeutics in AD model | 97 |

1. Introduction

1.1 Spatially resolved transcriptomics

Recent technological advances in omics have profoundly contributed to understanding biological discoveries. Instead of inferring the meaning through a few markers, the genome, transcriptome, or proteome in cells identifies the information in an unbiased way¹. New approaches have led to the discovery of novel prognostic, diagnostic, and therapeutic biomarkers and have been applied in various scientific fields to elucidate cellular heterogeneity and disease dynamics^{2,3}.

In neuroscience, research on various brain cells and pathological changes in aging or neurodegenerative disease has been actively conducted. For example, 25 brain cell types exhibited independent patterns of aging-related changes, and representative gene combinations have been identified⁴. Moreover, analysis of the choroid plexus, dura mater, and subdural meninges revealed immune diversity in the border region, especially in distinct subsets of border-associated macrophages with tissue-specific transcriptional signatures⁵. Further, transcriptional alterations associated with pathological progression have been identified cell-type-specifically from the prefrontal cortex of individuals with and without Alzheimer's disease (AD) pathology⁶.

As studies on changes in the gene expression of brain cells progressed, spatial and cellular heterogeneity of neurons and glial cells was revealed. Analysis of all cortical and hippocampal regions of adult mice showed the specificity of neurons based on brain structures⁷. Different subtypes of neurons were discovered in each layer of the isocortex. As the cortex and hippocampus

shared a common circuit organization, the neuronal subclasses of the hippocampus were also separated into types homologous to subsets found in the isocortex. Moreover, a highly diverse set of excitatory and inhibitory neuronal subclasses have been identified in the middle temporal gyrus of the human cortex⁸.

Glial cells are mainly categorized into lineages of astrocytes, oligodendrocytes, and microglia that support neuronal health, including synapse formation, neurotransmitters release and uptake, production of trophic factors, and control of neuronal survival⁹. Emerging evidence has shown astrocyte heterogeneity, revealing that different molecules and mechanisms control synapse formation in different brain regions¹⁰. For example, astrocytes from the adult mouse cortex and hippocampus were divided into distinct subtypes, which were in specific spatial position¹¹. Each astrocyte from different regions showed differential cell morphology and physiologies.

The transcriptional heterogeneity of oligodendrocytes was recently discovered. In particular, a distinct population of mature oligodendrocytes showed a spatial preference in the central nervous system (CNS)¹². According to the expression pattern, type 2 mature oligodendrocytes were enriched in the spinal cord, whereas types 5 and 6 functioned in all regions. Different types of oligodendrocytes showed different susceptibility to damage. Further, the functionally heterogeneous populations of oligodendrocytes have been found at a molecular level by the dynamics of differentiation and maturation¹³.

Lastly, specific time- and region-dependent subtypes of microglia during homeostasis and the changes in the subtypes in disease were revealed¹⁴.

Different subtypes of microglia have been identified with unique gene expression profiles over the course of development, from yolk sac progenitors to adult microglia. Strong variations between different regions have been found, indicating the regional specificity of microglia. In addition, in the cortex of patients with AD, disease-associated genes were markedly increased in certain microglial subpopulations¹⁵. The microglia surrounding the amyloid plaques have distinctive features compared to microglia located in other regions.

To understand the pathophysiology of the brain, it is important to consider the spatial complexity of representing interregional and intercellular dynamics throughout the regions. Several methods were introduced for a spatial description of brain cells, including fluorescence *in situ* hybridization¹⁶, immunofluorescence techniques¹⁷, and computational reconstruction using a reference database for spatial gene expression¹⁸. However, these approaches are incapable of providing information about the entire genes of the tissue.

A breakthrough for genome-wide exploration of tissue sections has resulted in the development of spatial barcode-based technology¹⁹. Although the current resolution has been improved to 100 micrometers, the method has an inherent limitation as a spot contains tens of cells inside. Nevertheless, Nature Methods selected spatially resolved transcriptomics (ST) as the method of the year in 2020²⁰. ST is currently being applied in various studies and has been judged to have great potential for development. As a suitable method for brain exploration, ST is a powerful method for anatomical information-based pathological comparative analysis that introduces an unbiased classification of spatial domains based on biological cues²¹.

1.2 Alzheimer's disease

AD is the most prominent neurodegenerative disease, accounting for 60-70% of all neurodegenerative disease cases worldwide. It mainly occurs in older adults over the age of 65, with the number of affected patients rapidly increasing in recent years²². The clinical classification of AD as a progressive disease is divided according to the pathological progression and cognitive ability²³. As severe cognitive impairment appears as a symptom and adversely affects the patient's quality of life, understanding and developing a treatment for AD is urgently needed.

The pathological hallmarks of AD are the accumulation of misfolded proteins such as amyloid plaques and abnormal tau tangles²⁴. The amyloid and tau toxicity cascade hypothesis suggests that the deposition of toxic protein aggregates drives pathological alterations such as neuroinflammation and oxidative stress, leading to neuronal damage. Disturbance of the excitatory and inhibitory synaptic balance may contribute to cognitive decline in AD²⁵. Several other hypotheses also propose the root cause of AD, including cholinergic deficiency, synaptic dysfunction, oxidative stress, and neuroinflammation²⁶. Regardless of the underlying cause of AD, all these factors aggravate disease progression.

Neuroinflammation in AD brains primarily involves pathologically altered glial cells and has been identified as a disease-risk factor²⁷. Upregulated activation levels of microglia and astrocytes were observed in patients with AD by positron emission tomography (PET)²⁸, and increased pro-inflammatory cytokines were also revealed in the serum, cerebrospinal fluid (CSF), and

postmortem brain of patients with AD²⁹. For example, the production of cytokines and chemokines, including IL-1 β , IL-6, IL-18, CCL1, CCL5, and CXCL1, was dramatically increased by innate immune cells in the CNS. The sustained inflammatory response extends to synaptic dysfunction, neuronal death, and inhibition of neurogenesis.

Immune dysfunction in AD has been considered a restricted issue in the CNS, but recent discoveries indicate a pivotal contribution of adaptive immunity to AD pathogenesis³⁰. Possible mechanisms of peripheral and central immune communication are divided into direct pathways involving peripheral immune cell infiltration and indirect pathways involving systemic inflammation-induced regulation of microglial function. Dysfunction of the blood-brain barrier (BBB) and blood-CSF barrier may enable cell entry into brain parenchyma³¹. Moreover, a recent discovery revealed that immune cells, such as T cells, B cells, monocytes, neutrophils, and natural killer (NK) cells, from skull bone marrow and blood are supplied to the meninges and enter parenchyma during injury or inflammatory response^{32,33}. Tissue-resident memory T cells contribute to inflammatory conditions in the CNS^{34,35}. Interestingly, CD4 T cells showed a conserved residency phenotype in the brain and were required for brain development by participating in the maturation of microglia³⁶. Intraventricularly injected CD4 T showed the interaction with microglia in the brain parenchyma of the AD model³⁷. Since microglial activation plays a major role in the cause of neuroinflammation, its association with peripheral immunity requires further investigation.

Impaired energy metabolism is one of the most consistent features of AD. As the brain is a high-energy consuming organ, even small changes in energy metabolism interfere with nerve function and impair cognitive abilities³⁸. Metabolism dysregulation is closely related to inflammatory responses. In AD, a metabolic shift in the microglia occurs from oxidative phosphorylation (OXPHOS) to glycolysis and is caused by acute beta-amyloid exposure³⁹. Then, activated microglia are enabled to perform energy-intensive processes such as proliferation, cytokine secretion, and phagocytosis. However, chronic exposure to toxic proteins results in defects in both OXPHOS and glycolysis, preventing sufficient energy supply. The metabolic reconfiguration of microglia and increased glucose uptake measured by 2-Dexoy-2-[¹⁸F]fluoro-D-glucose (FDG)-PET showed a positive correlation in the hippocampus⁴⁰. The FDG-PET signal is directly influenced by microglial glucose uptake than neurons and astrocytes. Patients with a neurodegenerative disease also exhibited an association of glucose uptake with microglial activity, indicating that performing FDG-PET can infer the microglial activation state⁴¹.

1.3 Pathological change of glial cells in AD

Glial cells in the AD brain have been difficult to isolate into specific subsets and define their roles at different stages of the disease. Recent advances in transcriptomes have made it possible to investigate highly complex pathological conditions, revealing cellular heterogeneity and disease dynamics.

In *App^{NL-G-F}* mice with progressive amyloid plaque accumulation, microglia were divided into three different states: homeostatic, interferon

response microglia, and activated response microglia (ARM)⁴². Notably, ARM were strongly enriched with AD risk genes, such as *Cst7*, *Clec7a*, *Lpl*, *Spp1*, and *Hif1α*. Moreover, the specific microglial subpopulation that appeared only in the AD mice compared to age-matched control mice was discovered and named disease-associated microglia (DAM)^{43,44}. DAM were generated in a two-step process. In the first step, homeostatic microglia genes such as *Cx3cr1* and *P2ry12* were downregulated, and in the second step, phagocytosis- and lipid metabolism-related genes including *Lpl*, *Cst7*, and *Axl* were upregulated. *Triggering receptor expressed on myeloid cells 2 (Trem2)* is essential for DAM activation from homeostatic microglia, specifically the transition from steps 1 to 2 DAM. During differentiation from homeostatic to DAM, microglia also subdivided into cell states belonging to distinct trajectories, interferon-responsive (IFN-R)-, cycling (Cyc-M)-, MHC-II expressing (MHC-II)-microglia, and DAM, that are expected to be involved in other signaling pathways⁴⁵. The gene expression pattern of microglia belonging to each trajectory changes depending on the presence of *Trem2* and sex.

Astrocytes are differentiated into reactive states and undergo morphological, molecular, and functional remodeling in response to injury, disease, or infection in the CNS⁴⁶. Neuroinflammation induced two different types of reactive astrocytes termed A1 and A2 subtypes⁴⁷. The A1 astrocytes showed an upregulation of classical complement cascade genes, which may be involved in the destruction of synapses. Astrocytes in the normal state are differentiated into the A1 subtype by microglia secreting *IL-1α*, *TNFα*, and *C1q*. However, the A2 astrocytes had increased neurotrophic factors, and it was

assumed that they were protective. The alteration of specific subtypes of astrocytes in AD was also identified and defined as disease-associated astrocytes (DAA)⁴⁸. DAA appeared at early disease stages and increased with disease progression. Notably, the DAA population showed an exclusively increased expression in the 5XFAD AD model compared to age-matched normal mice.

The function of activated microglia and reactive astrocytes in AD is still controversial⁴⁹. The glial cell-mediated clearance of beta-amyloid by phagocytosis or degrading enzymes was revealed in the AD model. Conversely, beta-amyloid and tau pathology induced an increase in inflammation pathway-related signatures in microglia and astrocytes, which induced a self-destructive environment by secreting chemokine and pro-inflammatory cytokines. Additionally, the synaptic density and dendritic morphology were impaired by complement signaling from glial cells.

1.4 AD therapeutics

Enormous efforts by the pharmaceutical industry are ongoing to develop therapeutics such as beta-amyloid-directed, tau-directed, and ApoE-directed therapeutics⁵⁰. Despite this, numerous failures in clinical trials have discouraged the development of drugs for AD. The United States Food and Drug Administration recently approved aducanumab, an anti-APP monoclonal antibody, as the first drug with a disease-modifying mechanism for AD⁵¹. More immunotherapeutics, including gantenerumab, lecanemab, and donanemab, have shown promising results from phase II clinical trials, and phase III studies

are currently underway⁵². Nevertheless, the approval of aducanumab has sparked a debate over its effectiveness. Although aducanumab exhibits a superior ability to remove amyloid plaques, which is considered the root cause of AD, the link between plaque reduction and cognitive improvement has not been demonstrated, and it is insufficient to explain many aspects of AD pathogenesis. Clinical data have not conclusively proven that aducanumab is effective in slowing cognitive decline. Accumulating evidence suggests that targeting the amyloid cascade alone cannot resolve diverse pathological processes^{53,54}. In recent genomics and functional studies, neuroinflammation was expected to be involved in the pathogenesis and progression of AD. The effect of improving cognitive ability in aged or AD mice was confirmed by regulating the glial cell activation state and cytokine signaling, but anti-inflammatory drug candidates have repeatedly failed in clinical trials⁵⁵. Various approaches are being used to find a cure for AD, but a limited understanding of the pathological mechanisms and methods to validate the effectiveness of treatment has limited any clear breakthroughs. Since AD is a multifactorial disease, it is necessary to investigate the global alterations that occur along with pathological progression.

1.5 Final goal of the study

In AD research, spatial spot-based analysis has been used to confirm plaque-associated genes that induce robust and coordinated responses in all cell types⁵⁶. Furthermore, genes involved in mitochondrial dysfunction were identified in the hippocampus and olfactory bulb⁵⁷. However, recent discoveries applying

spatial transcriptomics are still insufficient to understand pathological changes according to the anatomical brain regions of AD. This study aims to explore the AD model of different ages to understand spatiotemporal changes and validate the efficacy of therapeutics using NK cell supplements and anti-CD4 antibody (aCD4). These results are expected to provide therapeutic directions for AD, and the workflow demonstrated can be widely applied to various brain diseases to discover diagnostic and therapeutic targets.

2. Methods

2.1 Experimental models

2.1.1 AD models in different ages

Three-month- and 7.5-month-old male 5XFAD mice (Tg6799; on a C57/BL6-SJL background) containing five FAD mutations in human APP (the Swedish mutation, K670N/M671L; the Florida mutation, I716V; and the London mutation, V717I) and PS1 (M146L/L286V) and wild-type (WT) mice were used for spatially resolved transcriptomic data and immunofluorescence (IF) imaging. Mice of all strains were raised in a laboratory cage with controlled temperature and humidity and on a 12 h light-dark cycle with no restriction of standard feeding and water drinking. All experimental protocols and animal usage were approved by the Institutional Animal Care and Use Committee at Seoul National University.

2.1.2 Peripheral CD4 T cell blockade in AD model

Anti-CD4 antibody (0.5 mg/mouse; Bio X Cell) was intravenously injected to the 6.5-month-old 5XFAD and WT mice according to the groups. The samples of different tissues were obtained after a month. Coronal sections of brain samples were used for spatial transcriptomics and analyzed.

2.1.3 NK cell supplement in AD model

NK cells (2×10^6 cells/mouse in saline) were intravenously administrated once a week for a total of five times to the 6.5-month-old 5XFAD and WT mice. The

brain samples were obtained after five weeks and used for spatial transcriptome data.

2.2 Data Analysis

2.2.1 Spatial gene expression library construction

Brain hemispheres were prepared in frozen block using OCT compound (Sakura) and cryosectioned to 10 µm of coronal and sagittal sections. Prior to make Visium Spatial Gene Expression libraries, the permeabilization time should be optimized using Visium Spatial Tissue Optimization slides (10X Genomics) according to manufacturer's protocols. As the result, brain tissue was permeabilized for 12 min for Visium Spatial Gene Expression analysis. The brain sections were methanol-fixed, hematoxylin and eosin (H&E)-stained and imaged on a TissueFAXS PLUS (TissueGenostics). The slides were merged into a picture of the whole brain using TissueFAXS imaging software. Then, the sections were permeabilized and processed to obtain cDNA libraries. cDNA libraries were prepared according to the manufacturer's protocol. To verify the size of PCR-enriched fragments, I checked the template size distribution using high sensitivity DNA assay (Agilent Technologies 2100 Bioanalyzer).

2.2.2 Generation of count matrix

The libraries were sequenced using HiSeqXten (Illumina) with a read length of 28 bp for read 1 (Spatial Barcode and UMI), 10 bp index read (i7 index), 10 bp index read (i5 index), and 90 bp for read 2 (RNA read). Raw FASTQ data and

H&E images were processed by the Space Ranger v1.1.0 (10X Genomics) pipeline for the gene expression analysis of Visium spatial gene expression library data. Illumina base call files from the Illumina sequencing instrument were converted to FASTQ format for each sample using the ‘mkfastq’ command. Visium spatial expression libraries were analyzed with the ‘count’ command. Image alignment to predefined spots was performed by the fiducial alignment grid of the tissue image to determine the orientation and position of the input image. Sequencing reads were aligned to the mm10 reference genome (mm10-2020-A) using STAR (v2.5.1b) aligner. Gene expression profiling in each spot was performed with unique molecular identifier (UMI) and 10X barcode information.

2.2.3 Spatial transcriptome data: Integration and spot clustering

The generated gene counts were normalized using ‘LogNormalize’ methods with the scale factor 10,000 in Seurat v.3. The top highly variable genes (n= 2,000) were then identified using the ‘variance stabilizing transformation (vst)’ method in Seurat. The log-normalized count matrix was scaled, and principal component analysis (PCA) was performed for dimensionality reduction using the top highly variable genes. The number of RNA counts for each spot and the frequency of mitochondrial gene counts were regressed out in the scaling process. An integration was performed for multiple spatial datasets before spot clustering. A set of anchors were discovered between the datasets using ‘reciprocal PCA’ and normal mice (WT) were used as a reference during integration. The anchors were utilized to correct the count matrix in each spatial

data. Then, the corrected counts were integrated and were scaled and PCA was performed. For spot clustering, a shared nearest neighbor (SNN) graph was constructed, and the graph-based clustering was performed based on the Louvain algorithm. The resolution was set to 0.15. Markers for each cluster were identified by Wilcoxon rank sum tests for a given cluster versus other clusters implemented in Seurat as a FindAllMarkers function. The anatomical location of each cluster was visually identified by comparison with the Allen Mouse Brain Reference Atlas (<https://mouse.brain-map.org/static/atlas>). In all analyses, the count matrix normalized in the same way as above was used. For visualization, dimension reduction was performed using UMAP on the top 30 principal components. The spots with gene expression data were analyzed with the Seurat package (ver 4.1.1). For analysis of AD models in different ages, 14 spatial transcriptome datasets, composed of 48,480 spots with 32,885 genes in common, were integrated. For validation of therapeutic effect of NK cell and anti-CD4 antibody, 28 spatial transcriptome datasets, composed of 100,208 spots with 32,885 genes in common, were integrated and analyzed. All analyzes used data integrated and clustered by the above methods.

2.2.4 Differential gene expression analysis

MAST⁵⁸ in the Seurat function was used to perform differential gene expression analysis. Differentially expressed genes were extracted from the comparison of WT and AD model in each cluster. The cutoff of significantly different genes was FDR-adjusted $p < 0.05$ and $\log FC > 0.25$.

2.2.5 Gene ontology analysis

Gene ontology analyses were performed with clusterProfiler⁵⁹, which supports statistical analysis and visualization of functional profiles for genes and gene clusters. The Benjamini-Hochberg (BH) adjusted p-value was indicated. The ‘Enrichplot’ and ‘igraph’ package were additionally used.

2.2.6 Marker panel selection and curation

Necessary and Sufficient Forest (NS-Forest) version 2⁶⁰ was applied to the gene sets of the reference, *Ximerakis, 2019, Nature neuroscience*⁴. The brain cells from whole brain were classified with minimum features with high sensitivity and high specificity. For gene combinations identified in other references or mouse genome informatics (MGI), a panel of markers was constructed from individual gene curation. Genes that were not present in our spatial transcriptome data or expressed in less than 5 spots per sample were excluded.

2.2.7 Cellular signatures of reference data

Marker panels of reference papers were selected for the matrices of spatial transcriptomic data to calculate the signature score. The score was calculated with the AddModuleScore function with default parameters in Seurat. Each score was visualized by the SpatialFeaturePlot function for identifying spatial distribution patterns. The average expression level of the scores were calculated and the values were compared between WT and AD model in each brain region. The cutoff of significant differences between groups was Bonferroni-adjusted $p < 0.05$.

2.2.8 Spot-based correlation analysis

The score was calculated with the AddModuleScore function. Spearman correlation coefficients between the scores were identified and displayed on a heatmap or scatter plot.

2.2.9 Statistical analysis

For the spatial transcriptome data, plots in R were created either with the ggplot2 R package or Seurat modified by custom codes for data visualization. All p-values reported in this study were adjusted by false discovery rate and Bonferroni method.

2.3 Validation

2.3.1 Immunofluorescence imaging for tissue sections

Paraffin-embedded brain tissues were sectioned at 4 μm thickness. Deparaffinization was achieved with xylenes and decreasing concentrations of ethanol. Tissue sections were subjected to antigen retrieval using citrate buffer, pH 6.0, at boiling temperature for 10 min. Following rinsing with TBS, sections were incubated in blocking buffer containing TBS with 0.5% BSA for 1 h at room temperature. Slides were then incubated with primary antibody in blocking buffer overnight at 4 °C. The next day, slides were washed with TBS and then stained with Alexa Fluor secondary antibodies (Thermo Fisher Scientific). Sections were rinsed again and stained with DAPI (1:100; Invitrogen) before being cover-slipped with mounting medium. The primary antibodies used were mouse-6E10 (1:100; BioLegend), and rabbit-D54D2

(1:200; Cell Signaling). For the images of stained slide, the confocal microscopy (Leica TCS SP8) was used.

2.3.2 Behavior analysis, Y-maze

A Y-maze test was performed in each group of mice to evaluate spatial recognition memory using the natural exploratory behavior of mice. Mice were habituated to the behavior room and Y-maze, including background white noise the day before behavior analysis. The maze consisted of three arms converged in the central area of an equilateral triangle. Each mouse was placed at the center of Y-maze and allowed to move freely for 8 minutes. The number of arm entries were recorded to calculate the percentage of alternation.

2.3.3 NK cell isolation and culture

NK cells were isolated from spleen of BALB/c mouse according to the manufacturer's instructions for MACS cell separation with mouse NK cell isolation kit (Miltenyi Biotec). Isolated NK cells were incubated in RPMI-1640 supplemented with 10% fetal bovine serum (FBS) and 1% antibiotics-antimycotics in a 5% CO₂ atmosphere at 37 °C. Immediately after isolation and on day seven, cell viability was measured using trypan blue solution and viable cells were counted.

2.3.4 Flow cytometry for NK cell characterization

Isolated mouse NK cells were stained with target antibodies in flow cytometry staining buffer (Invitrogen) for 1 h. The cells were washed with buffer and

collected after centrifugation at 300 g for 5 min. The stained cells were placed in test tubes with FACS buffer. NovoCyte flow cytometer (Agilent) were used for analysis. Antibodies used for NK cell characterization were: CD3e-FITC (Invitrogen), NKp46 (CD335)-APC (BioLegend), CD19-APC (BioLegend), DNAM-1-PerCP-eFluor710 (BioLegend), CD107a-APC (BioLegend) and NKG2D (CD314)-PE (BioLegend).

2.3.5 IFN- γ and GM-CSF release assay by ELISA

Cultured media of NK cells were collected on days one and seven, and secretion of IFN- γ and GM-CSF was measured using a mouse IFN- γ and GM-CSF Quantikine ELISA kit (R&D systems) according to the manufacturer's instructions, respectively. The absorbance at 450 nm was measured using a Victor Nivo microplate reader (PerkinElmer). Results are expressed as pg/mL of cytokine.

2.3.6 Isolation of samples and live cell dissociation

Mice were anesthetized with isoflurane inhalation and perfused intracardially with cold Dulbecco's Phosphate-Buffered Saline (DPBS; Gibco). Whole brain, deep cervical lymph nodes, spleen and blood were removed.

Brain: The hippocampal regions were separated from the whole brain while keeping the temperature cool on ice. A papain dissociation system (Worthington biochemical corporation) was used for live cell dissociation according to the manufacturer's instruction.

dCLN: Both the right and left deep cervical lymph nodes were removed under stereomicroscope and placed into cold DPBS. The tissue was homogenized with a pestle and then the homogenized tissue in DPBS was passed through a 40 µm cell strainer (Corning). Cells were collected after centrifugation at 300 g for 5 min. The cells were placed in DPBS.

Spleen: The tissue was homogenized with a pestle and 1 ml of red blood cell lysing buffer (Sigma) was added. The solution was gently mixed and diluted with 10 ml of DPBS. Cells were collected after centrifugation at 300 g for 7 min. The cells were placed in DPBS and passed through a 40 µm cell strainer (Corning).

PBMC: Whole blood sample was obtained by retro-orbital blood collection after isoflurane anesthesia. PBMCs were isolated from blood by layering diluted blood (1:1 in DPBS) on top of an equal volume of Ficoll-Paque (Cytiva), followed by centrifugation at 400 g for 30 min and then isolation of the buffy coat. The cells were placed in DPBS.

2.3.7 MACS sorting of brain cells

Dissociated brain cells were collected in DPBS and T cells were isolated according to the manufacturer's instructions for MACS cell separation with mouse Pan T cell isolation kit and CD11b microbeads (Miltenyi Biotec). The MACS sorting was performed using an OctoMACS™ Separator and MS Columns (Miltenyi Biotec) according to the manufacturer's protocols.

2.3.8 Flow cytometry to verify the blocking effect of anti-CD4 antibody

Dissociated cells of blood, deep cervical lymph nodes, spleen, and brain were stained with target antibodies in flow cytometry staining buffer (Invitrogen) for 1 h. The cells were washed with buffer and collected after centrifugation at 300 g for 5 min. The stained cells were placed in test tubes with FACS buffer. Multicolor flow cytometry analysis was conducted using FACS Canto (BD Biosciences). Antibodies used to determine CD4 expression levels on isolated T cells and CD11b-positive cells were: CD3-APC-eFluor780 (Invitrogen), CD45-Super Bright 600 (Invitrogen), CD8a-PE (Invitrogen), and CD4 (GK1.5)-FITC (Invitrogen).

2.3.9 Statistical analysis

Experimental data were statistically analyzed with Prism software. Values were reported as average \pm standard deviation (SD). A comparative analysis was performed between two separate groups using the Wilcoxon rank sum test and among more than three groups using the Kruskal-Wallis one-way analysis of variance.

3. Results

3.1 Age-dependent change in the 5XFAD AD model

3.1.1 Analytical workflow for spatial transcriptome data

For a thorough investigation of brain tissue considering spatial heterogeneity, an analysis based on spatial transcriptomics (ST) is required. Here, I provide a workflow for determining biological differences between models using spot-based transcriptomic data (**Figure 1**) and a rich source for interpreting region-specific pathological properties in the AD mouse brain. First, I collected data from multiple groups and divided the brain regions to be analyzed using unsupervised clustering. Each cluster was named with anatomical information based on the Allen Mouse Brain Atlas. Then, the analysis was conducted in two ways: one analysis through differential expression (DE) analysis and the other analysis using reference-based marker panels.

I used MAST⁵⁸ for DE analysis which considers the bimodal expression profiles of single-cell transcriptome and utilizes the proportion of the detectable genes to discover biologically meaningful variations. As a result, differentially expressed genes (DEGs) and related biological pathways were identified for each cluster.

I also constructed a reference-based marker panel to validate changes in brain cell types or pathological conditions. Individual genes in the panel were curated, considering whether the gene was included in the gene lists of the ST data and whether the gene was expressed at a sufficient number of spots to identify significant differences. Further, Necessary and Sufficient Forest (NS-

Forest) version 2⁶⁰ was applied to the gene sets that identify diverse cell types in samples taken from whole mouse brains⁴ for minimum features with high sensitivity and high specificity for cell-type classification. A region-based comparative analysis of the average expression and correlation analysis was performed using the panel of identified markers.

A key feature of the spot-based data presented here is that each cluster represents a region in which various molecular and cellular changes are investigated. Moreover, variations exist in the number of spots included in clusters according to the location of the tissue sections. Thus, I compared the mean expression of selected gene sets to correct the number of spots and the variation between biological replicates.

Resultantly, the workflow for spot-based transcriptomic analysis is expected to facilitate the discovery of alterations in region-specific DEGs and cell- and state-associated gene distribution according to the disease progression.

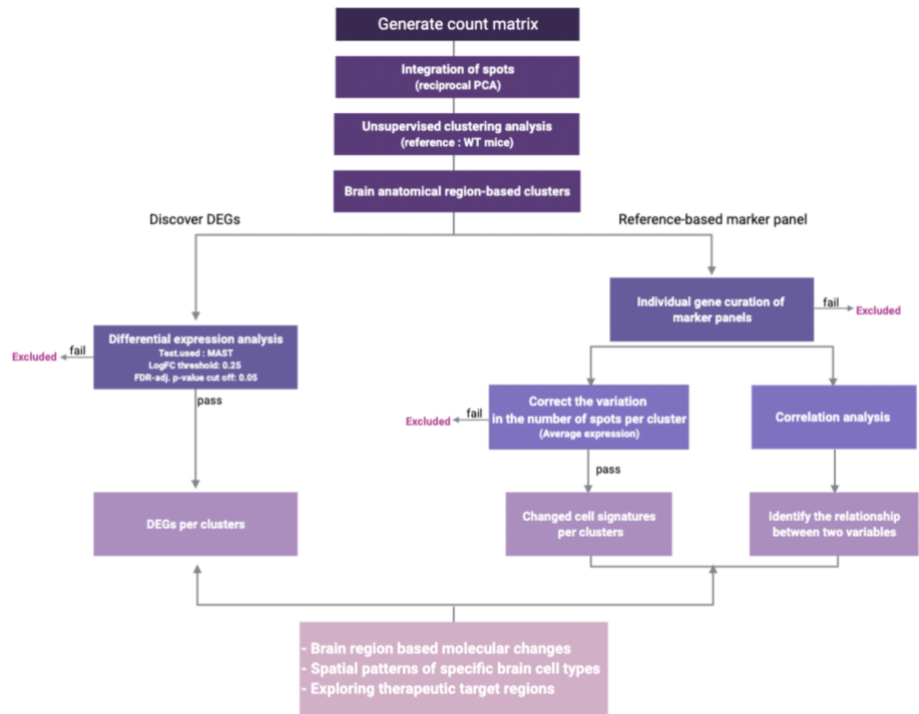


Figure 1. Schematic workflow to identify differences between groups using spatial transcriptome data.

Schematic diagram of the workflow conducted in this study. Criteria are specified for each analysis. Genes that did not meet the criteria were excluded.

3.1.2 Identifying clusters corresponding to anatomical structures of the brain

To investigate regional changes in pathological progression in AD, I obtained ST data from the AD model of 5XFAD (TG) and age-matched wild type (WT) mice at three- and 7.5-month-old. Coronal sections at approximately bregma 1.94 mm were obtained (**Figure 2A**). A total of 48,480 spots containing 32,285 messenger ribonucleic acid (mRNA) expression data were used for unsupervised clustering analysis, and the brain regions were defined. The names of the identified 11 clusters were assigned according to the corresponding brain anatomy in 14 samples: thalamus, hypothalamus, deeper cortex, upper cortex, hippocampus, white matter, striatum, amygdala, and the pyriform area, ventricular area, border region, and reticular nucleus of the thalamus (**Figure 2B**). The result revealed the advantage of ST being able to classify brain regions without intentional segmentation. The spot clusters were represented by a uniform manifold approximation and projection (UMAP) plot, a dimensionality reduction method for visualization⁶¹, and the clusters, representing each brain region, were well separated in terms of gene expression. Then, the spots from each group were color-coded on the UMAP. The groups largely overlapped, which implies that the batch effect was minimized (**Figure 2C**). The top five genes of the clusters were extracted and visualized with a heatmap, demonstrating that representative genes are exclusively high in that region (**Figure 2D**). The number of spots between samples in each region is similar, and the number of spots per sample in the hypothalamus, thalamus, cortex, hippocampus, white matter, striatum, and amygdala clusters is 150 or

more, which is sufficient to find a meaningful result (**Figure 2E**). Thus, eight brain regions were selected as the main analysis targets, and changes according to pathological progression in the AD model were confirmed at the molecular level.

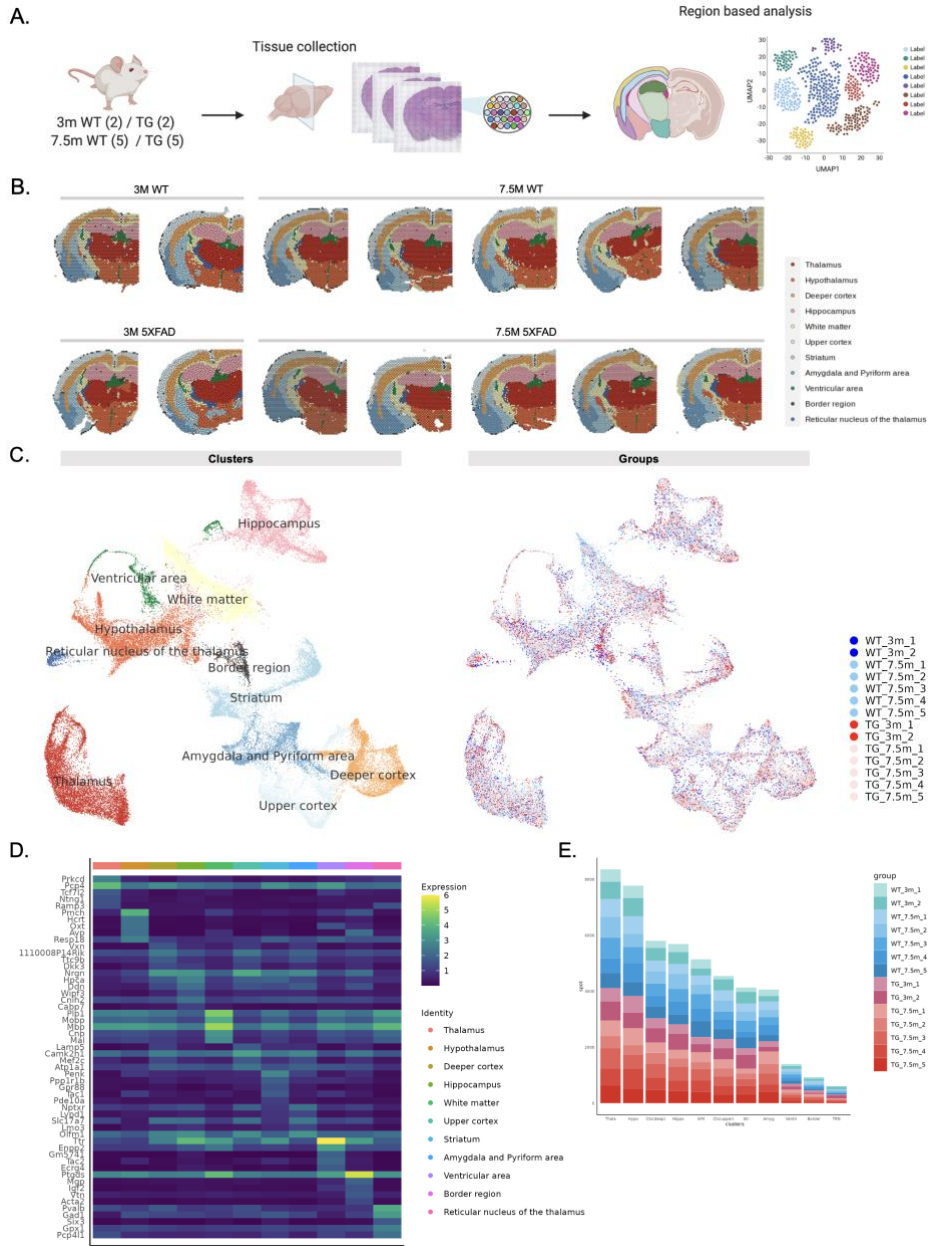


Figure 2. Spatial transcriptome-based cluster analysis in the three-month- and 7.5 month-WT and AD model.

(A) Schematic overview of the experimental workflow for spatial transcriptome data in the WT and AD model at three and 7.5 months old. (B) Eleven clusters were identified according to 14 mice in each of the WT and AD model of

different ages. Coronal sections were used in each group. The clusters were colored and annotated based on the anatomical brain regions. (C) UMAP of 48,480 spots. The clusters were colored and annotated based on the information obtained in b (left). A UMAP plot was colored with each group. The blue dots indicate two mice in the three-month-old WT group, the light blue dots indicate five mice in the 7.5-month-old WT group, the red dots indicate two mice in the three-month-old WT group, and the pink dots indicate five mice in the 7.5-month-old AD model (right). Each dot represents the transcriptomic data of each spot. (D) Heatmap showing the distribution of expression levels of marker genes across 11 brain region-based clusters. The top five genes were identified for each cluster. (E) The total number of spots per cluster was plotted as a bar plot. (Wild type: WT; 5XFAD AD model: TG)

3.1.3 Investigation of DEGs in the AD model of different ages groups

A 5XFAD AD model is known to show amyloid deposition and reactive gliosis from two months and synaptic loss and cognitive impairment from four to six months⁶² (**Figure 3A**). I obtained adjacent coronal sections to the section processed for ST and confirmed the amyloid deposition (**Figure 3B**). Only a small portion of beta-amyloid was observed in the white matter, deeper cortex, and thalamus in the three-month-old AD model, whereas a dramatic increase was found mainly in the deeper cortex, white matter, thalamus, and amygdala in the 7.5-month-old AD model.

I subsequently identified a difference between the AD model before and after accumulation of definite amyloid plaques using ST. I first analyzed DEGs in specific brain regions of the three-month- and 7.5-month-old AD model compared to age-matched WT mice. Of the 1,670 total DEGs in the three-month-old AD model, the region with the most gene changes was the white matter (1,320 genes), and fewer than 100 genes were identified in the gray matter. In the AD model at 7.5 months, most genes were still identified in the white matter (611 genes) among 1,213 DEGs. However, in the three-month AD model, the changes in the genes in the gray matter were increased. Among the gray matter, the most DEGs were identified in the thalamus (182 genes), and the second was the deeper cortex (102 genes). It was found that there was a noticeable change in the gene level of the white matter before definite accumulation of amyloid plaques, and there was an overall change in the gray and white matter after definite amyloid pathology progressed in the AD model.

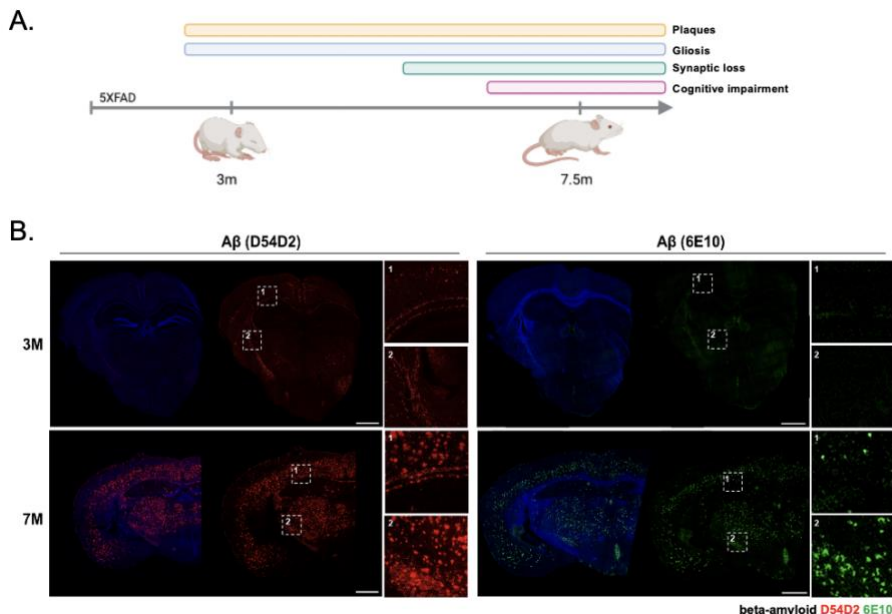


Figure 3. Distinctive expression pattern in the three- and 7.5-month-old WT and AD model.

(A) Schematic overview of the age-dependent phenotypic characterization of the 5XFAD AD model. (B) Immunofluorescence images for the coronal sections of the three-month- and 7.5-month-old 5XFAD mice obtained from the same brain samples used for ST ($n=3$). Beta-amyloid was stained with D54D2 antibody (left; red) and 6E10 antibody (right; green). Inset 1 indicates the corpus callosum and cortex, and 2 indicates the internal capsule and thalamus. Scale bars, 1 mm.

3.1.3.1 DEGs and related biological pathways in three-month-old AD model.

I investigated the upregulated and downregulated transcriptional changes in three-month-old AD model compared to WT. First, I compared DEGs in the white matter, thalamus, hippocampus, and upper cortex, where a relatively large number of genetic changes were identified (**Figure 4A, B**). In both increased and decreased DEGs in AD model, most genes were identified exclusively in the white matter, with fewer than 20 genes found in each gray matter region. Genes upregulated in the white matter of AD model compared to WT included *Tmem242*, *Hsd17b12*, *Ctss*, *Cops4*, *Mrpl51*, *Llph*, *Arpc1b*, *Tial1*, *Aebp2*, and *Rbis*, in order of the fold change values. The downregulated genes included *Camkk1*, *Sndl*, *Rab15*, *Bc1*, *Nrd1*, *Itpa*, *Trak1*, *Hpcal4*, *Cyfip1*, and *Fabp3* (**Figure 4C**). Then, I identified the related biological pathways of the DEGs that were specifically detected in the white matter region. Genes upregulated in AD model were associated with functions such as gliogenesis and glial cell differentiation (**Figure 4D**). The DEGs related to gliogenesis and glial cell differentiation in the three-month-old AD mice were *9630013A20Rik*, *Abca2*, *Abll*, *Actr3*, *Arhgef10*, *Aspa*, *Bin1*, *Cnp*, *Cntn1*, *Gfap*, *Il33*, *Il6st*, *Mag*, *Mapk3*, *Metrn*, *Myrf*, *Nkx6-2*, *Olig1*, *Opalin*, *Phgdh*, *Plp1*, *Psen1*, *Ptn*, and *Tspan2*. In addition, functions related to synapse organization and vesicle-mediated transport in the synapse were decreased with increased gliogenesis, particularly in the white matter. Changes predominately occurred in the white matter rather than in other brain regions in the early stage of AD pathology.

3.1.3.2 DEGs and related biological pathways in 7.5-month-old AD model.

The 7.5-month-old AD model with accumulation of definite amyloid plaques were compared with age-matched WT mice to identify the upregulated and downregulated DEGs. As in three-month-old AD model, DEGs were found the most in the white matter. However, the number of DEGs in the gray matter was remarkably increased at 7.5-months of age (**Figure 4E, F**). The thalamus was the region where the most changed genes were found among the gray matter of AD model. Then, I confirmed DEGs and the related biological pathways in the white matter and thalamus (**Figure 4G**). The genes upregulated in the white matter of 7.5-month-old AD compared to WT mice included *Ctsd*, *Tyrobp*, *Eif6*, *Ftl1*, *Cst7*, *Hexb*, *Lyz2*, *Serpina3n*, *Gfap*, and *C4b*, in order of the fold change values. The downregulated genes included *Mapk9*, *Ldha*, *Gsk3b*, *Ndflp2*, *Nsa2*, *Rfc2*, *Rbm5*, *Iffo1*, *Ablim2*, and *Nefl*. The upregulated genes are mainly associated with gliogenesis, glial cell differentiation, glial cell proliferation, macrophage proliferation, and microglial cell activation (**Figure 4H**). The genes involved in glial cell-related biological pathways are *Csf1*, *Csf1r*, *Cx3c1l*, *Dbi*, *Gfap*, *Nf2*, *Aif1*, *Cst7*, *Tyrobp*, *C1qa*, *Clu*, *Eif2b2*, *Gpr3711*, *Grk2*, *Grn*, *Hdac11*, *Ilk*, *Nlgn3*, *Ntrk2*, *Pmp22*, *Serpine2*, *Stat3*, *Tmem98*, *Trem2*, and *Vim*. Conversely, the downregulated genes are linked to proteasomal protein catabolic process, mitochondrion organization, and locomotory behavior in the white matter of 7.5-month-old AD model.

The DEGs of the thalamus region were confirmed in the 7.5-month-old AD model. The upregulated genes were *Gfap*, *Ctsd*, *Tyrobp*, *Ftl1*, *Serpina3n*,

Cst7, *Ctss*, *C1qa*, *Hexb*, and *Apoe*, in order of the fold change values. The downregulated genes were *Tmsb10*, *Bc1*, *Ndufv3*, *Rpl29*, *Gng13*, *Uba52*, *Atp5j2*, *Malat1*, *Atp5md*, and *Cox7c*. The upregulated genes are related to gliogenesis, astrocyte development, and microglial cell activation, which are also involved in the function of white matter. The involved genes in the glial cell-related biological pathways are *Atp1b2*, *C1qa*, *Cd9*, *Clu*, *Cnp*, *Csf1r*, *Cx3cr1*, *Dbi*, *Gfap*, *Gpr37l1*, *Grn*, *Hexb*, *Plp1*, *Trem2*, *Trf*, *Vim*, *Cst7*, and *Tyrobp*. Thus, in 7.5-month-old AD model, the white matter and genes in the thalamus revealed increased glial cell activation. Interestingly, in contrast to the white matter, a remarkable increase in antigen processing and the presentation-related pathways was also confirmed in the thalamus. The related genes are *B2m*, *Cd68*, *Ctsl*, *Ctss*, *Fcer1g*, *Fcgr2b*, *Fcgr3*, *H2-D1*, *H2-K1*, and *Trem2*. The association with adaptive immunity may be considered in the thalamus of the gray matter rather than the white matter. In contrast, the downregulated genes associated with the gene ontology (GO) pathways were the adenosine triphosphate (ATP) metabolic process and oxidative phosphorylation.

Consequently, the biological pathways of gliogenesis and glial cell activation were upregulated mainly in the white matter of three-month-old AD model and the white and gray matter of 7.5-month-old AD model. However, the involved genes were age- and region-specifically identified. Only *Gfap*, which encodes one of the major intermediate filament proteins of mature astrocytes, was commonly identified and most of the individual glial cell-related genes were increased specifically for each group. There were more commonly involved genes among regions within the 7.5-month-old AD model.

The genes were *Csf1r*, *Dbi*, *Cst7*, *Tyrobp*, *C1qa*, *Clu*, *Trem2*, and *Vim*. Moreover, *Cnp* and *Plp1* were upregulated in both the white matter at three months and the thalamus at seven months old in AD model. Except for those genes, glial cell-related genes increased independently in each group. The genes exclusively increased in the white matter of three-month-old AD model were *9630013A20Rik*, *Abca2*, *Abl1*, *Actr3*, *Arhgef10*, *Aspa*, *Bin1*, *Cntn1*, *Il33*, *Il6st*, *Mag*, *Mapk3*, *Metrn*, *Myrf*, *Nkx6-2*, *Olig1*, *Opalin*, *Phgdh*, *Psen1*, *Ptn*, and *Tspan2*. Furthermore, the genes in only the white matter of 7.5-month-old AD model were *Csf1*, *Cx3cl1*, *Nf2*, *Aif1*, *Cx3cl1*, *Eif2b2*, *Gpr3711*, *Grk2*, *Hdac11*, *Ilk*, *Nlgn3*, *Ntrk2*, *Pmp22*, *Serpine2*, *Stat3*, and *Tmem98*, and in only the thalamus were *Atp1b2*, *Cd9*, *Cx3cr1*, *Gpr3711*, *Hexb*, and *Trf*. Although similar biological pathways were enriched across the different regions and ages, the key altered gene combinations were distinct from each other.

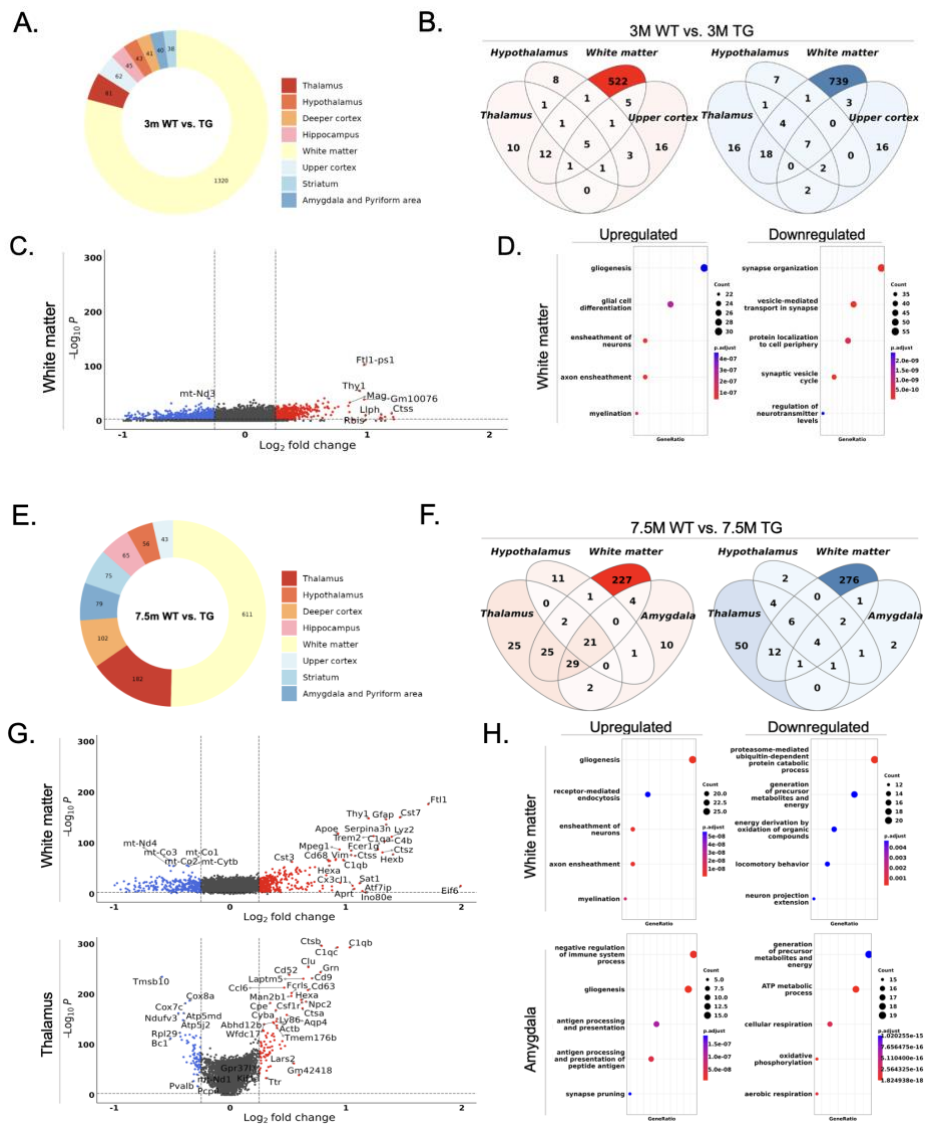


Figure 4. Identification of DEGs and related biological pathways in the AD model at three and 7.5 months compared to WT mice.

(A) Pie chart demonstrating the DEG proportion of AD model compared to WT at three months in each brain region. The number of genes detected in each region out of 1,670 genes (three months) is displayed in color-coded regions.

(B) Venn diagram representing the upregulated (left; red) and downregulated (right; blue) DEGs in the three-month-old AD model compared to WT mice.

The regions with the most genes are expressed in dark colors. (C) Volcano plot for the genes identified in the three-month-old AD model compared to the WT mice in the white matter. The genes in the colored dots are significantly ($\log_{10}FC$ threshold = 0.25) upregulated (red dots) and downregulated (blue dots). The dots colored dark gray represent the genes that were not significantly changed in AD model. (D) The top five GO terms related to the upregulated (left) and downregulated (right) genes in the three-month-old AD model compared to WT mice in the white matter. (E) Pie chart demonstrating the DEG proportion of AD model compared to WT at 7.5 months (right) in each brain region. The number of genes detected in each region out of 1,213 genes (7.5 months) is displayed in color-coded regions. (F) Venn diagram representing the DEGs in the 7.5-month-old AD model compared to WT mice. (G) Volcano plot for the genes identified in the 7.5-month-old AD model compared to the WT mice in the white matter and thalamus. (H) The top five GO terms in the 7.5-month-old AD model compared to WT mice in the white matter and thalamus. An initial change of glial cell-related biological pathways occurs in the white matter prior to the distinct changes in the gray matter.

3.1.3.3 Changes by brain regions according to the progression of amyloid pathology in AD model.

Alterations according to pathological progression were investigated by comparative analysis of AD models of different ages (three- and 7.5-month-old AD model). There are two main changing factors: pathological changes by the accumulation of beta-amyloid in the 5XFAD AD model and age-related changes. To separate the two factors, I compared the upregulated and downregulated DEGs at 7.5-months compared to three-months of age in the WT and AD model. Most of the DEGs belonged specifically to each group rather than overlapping between the two groups of mice. The highest number of DEGs was observed in the white matter. The top 20 genes and their associated GO terms that were differentially expressed in WT at 7.5-months of age compared to three-months are listed in **Table 1**.

Genes overlapping between the WT and AD model were excluded from DEGs in the AD model so as to confirm only the changes according to AD progression except for differences due to age. The top 20 DEGs and the related biological pathways are listed in **Table 2**. Then, we investigated the upregulated and downregulated transcriptional changes in the white matter, amygdala, deeper cortex, and striatum (**Figure 5A, B**). In the white and gray matter, the number of overlapping DEGs was relatively high in the upregulated genes, and there were fewer than 10 overlapping genes in the downregulated genes. The genes upregulated in the white matter and amygdala were identified (**Figure 5C**) and both regions commonly revealed increased glial cell-related biological pathways (**Figure 5D**). Further, I identified the interregional associations of

increased and decreased gene-related GO terms of the main brain regions (**Figure 5E**). The top five upregulated functions by region are all involved in the proliferation and activation of glial cells. In particular, the DEG-related pathways in the deeper cortex, hippocampus, striatum, and amygdala were more closely related. However, the function associated with the downregulated genes showed a regional-specific tendency. The biological pathways related to mitochondrial function were remarkably downregulated in the thalamus and white matter, whereas downregulated genes in the hippocampus and deeper cortex were commonly associated with intercellular protein transmembrane transport. The decrease in functions related to learning or memory and cognition was prominently identified in the amygdala, and a decrease in genes related to neurotransmitter-related pathways was identified in the hypothalamus regardless of other regions. Despite the overall increase in the activity of glial cells, function deterioration due to the progression of AD differed for each region according to the spatial heterogeneity of the brain.

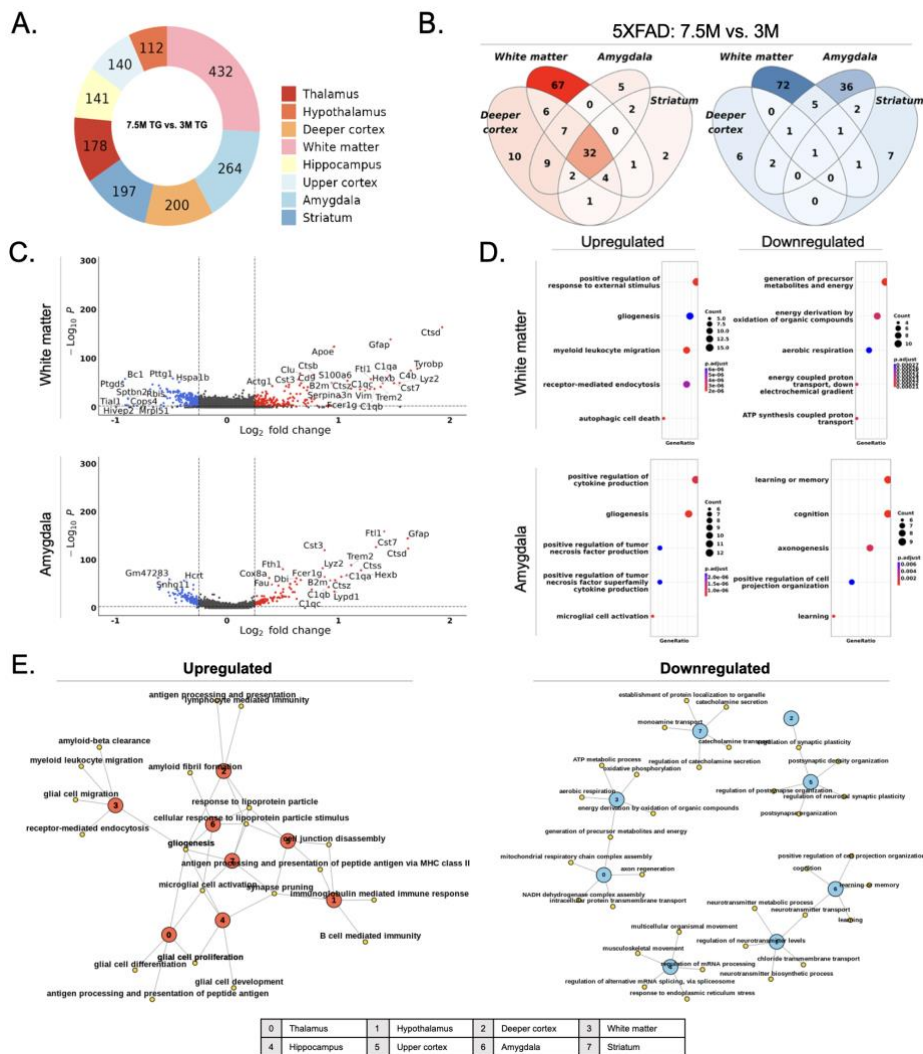


Figure 5. Regional changes in AD model from three months to 7.5 months

(A) Pie chart demonstrating the DEG proportion of 7.5-month-old AD model compared to three-month-old AD model in each brain region. (B) Venn diagram representing the upregulated (left; red) and downregulated (right; blue) DEGs in the 7.5-month-old compared to three-month-old AD model. The regions with the most genes are expressed in dark colors. (C) Volcano plot for the genes identified in the 7.5-month-old compared to three-month-old AD

model in the white matter and amygdala. The genes in the colored dots are significantly (logFC threshold = 0.25) upregulated (red dots) and downregulated (blue dots). The dots colored dark gray represent the genes that were not significantly changed in AD model. (D) The top five GO terms related to the upregulated (left) and downregulated (right) genes in the white matter and amygdala. (E) GO network based on genes that change by AD progression, excluding the changes by age difference. The red nodes represent the clusters with upregulated GO terms, and the blue nodes represent the downregulated GO terms. The yellow nodes represent each biological pathway. The upregulated pathways show the interregional associations, while the downregulated pathways show regional-specific expression patterns.

Table 1. Representative genes and biological pathways that change

regionally in 7.5-month-old compared to three-month-old WT mice.

The top 20 upregulated and downregulated DEGs are listed in order of the fold change values (FDR-adj. p-value < 0.05, logFC threshold = 0.25). The top five GO terms considering the p-value and number of involved genes are listed.

Table 2. Representative genes and biological pathways that change

regionally in the 7.5- compared to the three-month-old AD model.

excluding the age-dependent changes in WT mice.

The top 20 upregulated and downregulated DEGs are listed in order of the fold change values (FDR-adj. p-value < 0.05, logFC threshold = 0.25). The top five GO terms considering the p-value and the number of involved genes are listed.

3.1.4 Spatial distribution of diverse cell signatures in the AD model.

I applied known brain cell signatures to estimate regional cell distribution. Firstly, I used the gene sets representing 25 brain cell types⁴ with distinct expression profiles, applying Necessary and Sufficient Forest (NS-Forest)⁶⁰ for minimum features with high sensitivity and high specificity for cell-type classification. I selected representative 7.5-month-old WT and AD model that reflected the average expression level and then identified the regional changes in the spatial patterns of diverse brain cells (**Figure 6A**). Each cell type showed a region-specific expression pattern. For example, neuron-related signatures (NSF_mNeur) were expressed mainly in the gray matter, and oligodendrocyte-related markers (NSF_olig) were remarkably expressed in the white matter. Additionally, the signatures of neuroendocrine cells (NSF_NendC) were found in the hypothalamus, and choroid plexus cells (NSF_CPC) were in the ventricular area.

The gene sets of cell types with the most pronounced changes in AD model were microglia (NSF_mg), astrocyte-restricted precursors (NSF_ARP), and macrophage (NSF_MAC). A common spatial pattern change observed in these cells was that expression was found only in the white matter in WT mice, whereas expression was dramatically increased across most of the regions in AD model. Conversely, it was observed that the expression level of neuronal signatures (NSF_mNeur, NSF_NRP) was generally reduced in all regions in AD model compared to WT mice. Then, I compared the correlation between spots expressing each of the 25 cell signatures in 7.5-month-old AD model (**Figure 6B**). As a result, high positive correlations among glial cell-related

signatures and negative correlations between neurons- and glial cell-related genes were confirmed. Since glial cells and neurons in AD model are inversely proportional, an association can be inferred between neuronal loss and rapid increases in microglia, macrophage, and astrocytes.

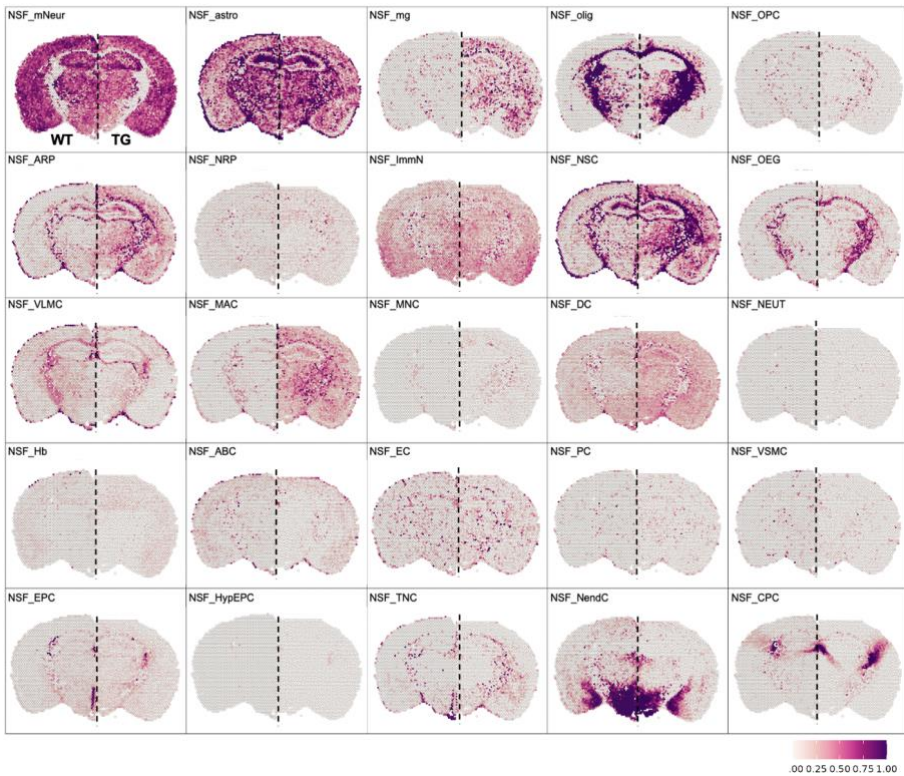
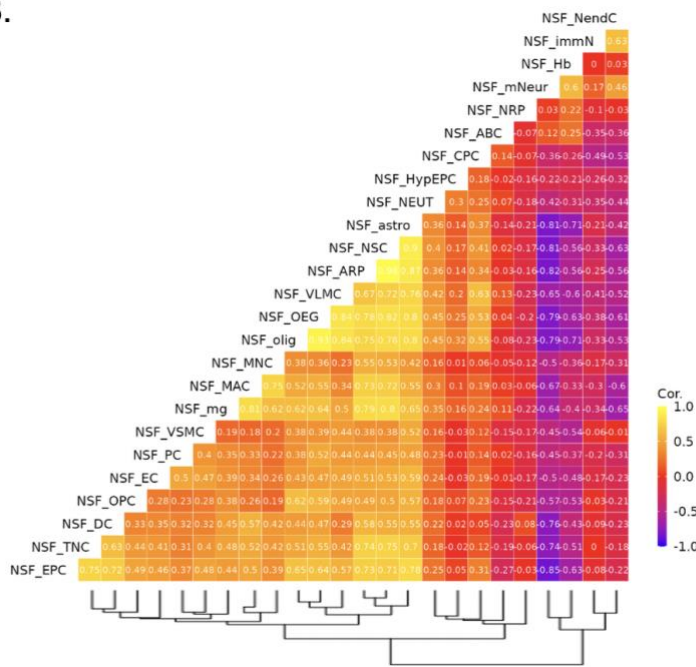
A.**B.**

Figure 6. Identification of spatial changes in the distribution of diverse brain cells in 7.5-month-old WT and AD model.

(A) Spatial patterns of 25 types of brain cell signatures. The left side of the hemisphere is representative of WT, and the right side is representative of AD model. NSF_mg, NSF_ARP, and NSF_MAC showed the most significantly increased patterns in the AD model. The scale bar is matched from 0 to 1 for all spatial features. (B) Correlation graph demonstrating the relationship between 25 brain cells in AD model. The correlation values are specified in each box, and the different colors also express the relative degree. A distinction was made between the groups of cell signatures in which spatial patterns were closely or less related. (NSF_mNeur: mature neuron; NSF_astro: astrocytes; NSF_mg: microglia; NSF_olig: oligodendrocyte; NSF_OPc: oligodendrocyte precursor cells; NSF_ARP: astrocyte-restricted precursors; NSF_NRP: neuronal-restricted precursors; NSF_immN: immature neurons; NSF_NS: neural stem cells; NSF_OEG: olfactory ensheathing glia; NSF_VLMC: vascular and leptomeningeal cells; NSF_MAC: macrophage; NSF_MNC: monocytes; NSF_DC: dendritic cells; NSF_NEUT: neutrophils; NSF_Hb: hemoglobin-expressing vascular cells; NSF_ABC: arachnoid barrier cells; NSF_EC: endothelial cells; NSF_PC: pericytes; NSF_VSMC: vascular smooth muscle cells; NSF_EPC: ependymocytes; NSF_HypEPC: hypendymal cells; NSF_TNC: tanycytes; NSF_NendC: neuroendocrine cells; NSF_CPC: choroid plexus epithelial cells)

3.1.4.1 Spatial distribution of the subtypes of glial cell signatures in AD model.

I investigated the expression patterns of glial cell signatures, including microglia, astrocyte, and oligodendrocytes, known as major players in the progression of neuroinflammation. First, I validated altered regional expression in AD model compared to WT using various reference-based microglial signatures (**Figure 7A**). A dramatic increase in the white matter was observed at three months of age, and an overall increase was observed at 7.5 months in AD model. Then, I used the signatures of microglial subtypes (homeostatic and disease-associated microglia) to identify the specific type that contributed most to altered expression patterns (**Figure 7B**). The spatial pattern of disease-associated microglia (DAM) signatures^{43,44} was increased only in the white matter in three-month-old AD model, and in 7.5-month-old AD model, the expression level was increased significantly in all regions. Interestingly, there was also a marked increase in the signature of homeostatic microglia in most regions except for the hypothalamus and white matter regions, but the changes in the expression level in the early stage of AD were insignificant. Thus, only activated microglial signatures revealed the early change in the white matter and then dramatically increased in all regions with disease progression.

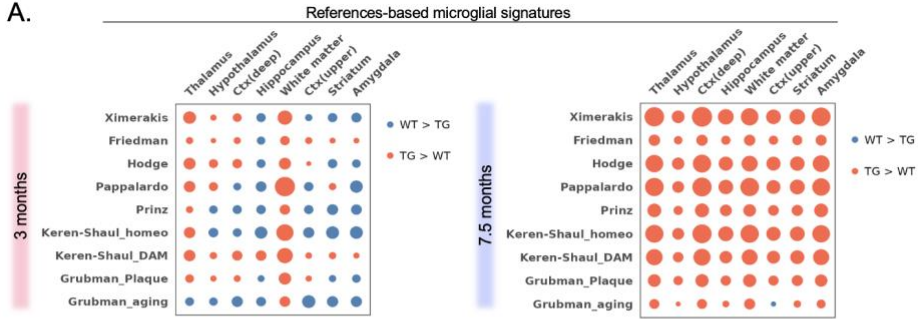
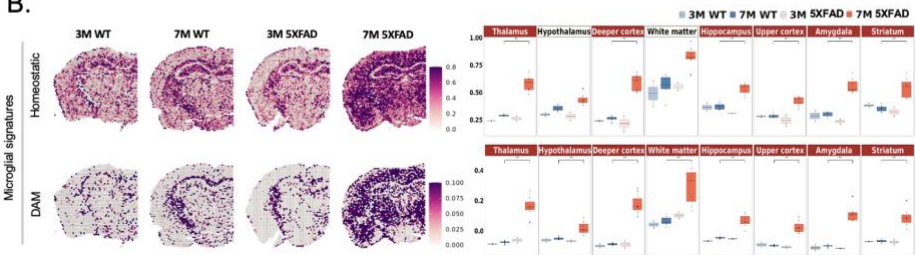
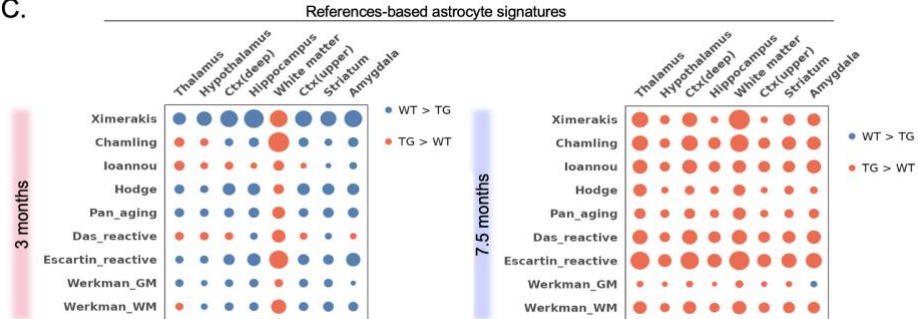
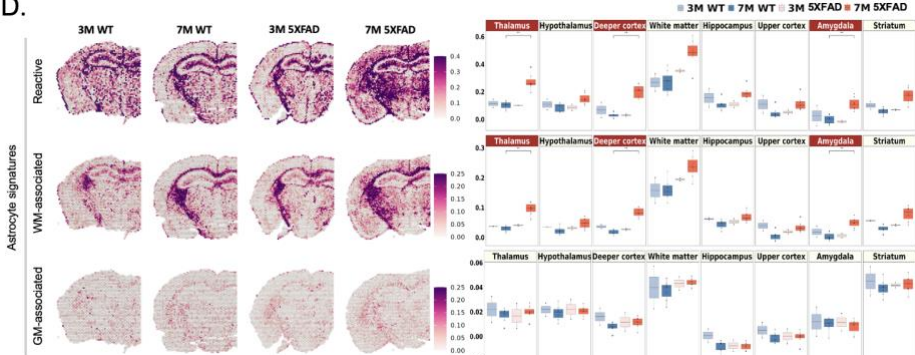
For astrocytes, I compared several reference-based astrocyte signatures between the WT and AD model at three- and 7.5-months of age (**Figure 7C**). Similar to the microglial cell signatures, an exclusive increase in the white matter at three-months and an overall increase at 7.5-months of age in AD model was confirmed. I then used three different gene sets^{46,64,65} to subdivide

the astrocyte signatures in different states, representing reactive, white matter associated, and gray matter associated astrocytes, respectively (**Figure 7D**). Reactive astrocyte-related genes showed relatively high expression in the white matter, even in WT mice. Nevertheless, the expression in three-month-old AD model showed a tendency to increase in the white matter compared to age-matched WT mice. In 7.5-month-old mice, the expression of reactive astrocytes-related genes revealed significant increases in the thalamus, deeper cortex, and amygdala. The spatial distribution of white matter associated astrocyte signatures rather than gray matter associated astrocyte showed an expression pattern that correlated with reactive astrocyte signatures. Astrocytes in the white matter may be the main subtype that changes to reactive status with the progression of amyloid pathology.

Oligodendrocyte signatures validated using several reference paper-based markers also showed a similar expression pattern in AD model compared to WT, but the difference was insignificant (**Figure 7E**). Recently, the heterogeneity of oligodendrocytes was identified by analyzing single-cell transcriptome data obtained from oligodendrocyte lineage¹³. The signatures of oligodendrocytes were divided into five subtypes: Mature_olig, Myelin_olig, New_olig, COP (committed oligodendrocyte progenitors), and OPC (oligodendrocyte precursor cells). However, compared to microglia and astrocyte signatures, there was no significant change in the white matter where oligodendrocytes were most expressed at three-months in AD model. An increase was observed in the mature oligodendrocyte signatures in the deeper

cortex of 7.5-month-old AD model, but the overall expression level was low to evaluate the significance of the change (**Figure 7F**).

Among glial cells, microglia and astrocyte signatures in the white matter are markedly increased in the early stage of AD, and these altered expression patterns also affected the gray matter as the disease progresses.

A.**B.****C.****D.**

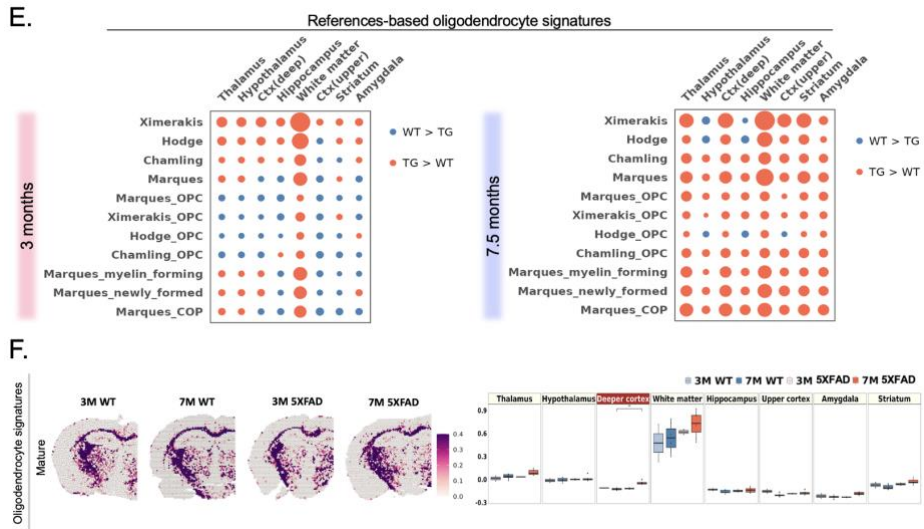


Figure 7. Spatial changes in the distribution of glial cell subtypes in AD models at different ages.

(A) Dot plot showing the average expression differences of various reference-based microglial cell signatures in each region. Expression differences between the three- (left) and 7.5-month-old (right) WT and AD model were indicated. Based on the AD model, the blue dot indicates a decrease, and the red dot indicates an increase. The size of the dots is proportional to the average expression difference value. (B) Spatial pattern of the signatures of DAM (left) and the boxplot showing the average expression levels (right). Each dot represents a mouse in each group. (C) Dot plot showing the average expression differences of various reference-based astrocyte signatures in each region. (D) Spatial pattern of the signatures of reactive astrocyte, white matter associated, and gray matter associated microglia (left) and the boxplot showing the average expression levels (right). (E) Dot plot showing the average expression differences of various reference-based oligodendrocyte signatures in each region. (F) Spatial pattern of the signatures of mature oligodendrocyte (left) and

the boxplot showing the average expression levels (right). The average expression level of DAM and reactive astrocyte signatures (indicated in pink boxes) showed a tendency to increase in the white matter of the AD model at three months, with a clear increase at 7.5 months. [#]Bonferroni-adj. p-value < 0.05 (compared to age-matched WT mice). (7.5-month-old: 7M, 7.5M)

3.1.4.2 Spatial distribution of myeloid and lymphoid cell signatures in AD model.

Increasing evidence suggests the contribution of neuroimmune crosstalk between the brain and peripheral immune system to the pathogenesis of AD^{29,31,32}. Peripheral myeloid and lymphoid cells may enter the tissue parenchyma and change the glial cell activation status. I investigated changes in immune cells, which are rare in the brain. First, the reference-based signatures of diverse subtypes of myeloid cells, including CNS-associated macrophages (CAM), macrophages, monocytes, myeloid dendritic cells (DCs), plasmacytoid DCs, and granulocytes, were evaluated and revealed an increased tendency in AD model compared to WT (**Figure 8A**). In particular, the expression of macrophage, monocyte, DCs, and granulocyte signatures tended to increase throughout the regions of 7.5-month-old AD model compared to the expression confirmed only in the white matter region in WT and three-month-old AD model (**Figure 8C**).

The expression level of signatures of natural killer (NK) and T cells was compared between groups. NK cells were subdivided into different subtypes: tissue-resident memory NK cells, infiltrated NK cells, CD56-bright, and -dim NK cells (**Figure 8B**). In the case of the CD56-dim NK cell signatures, the genes were expressed in the white matter, hippocampus, and thalamus regions. The expression level of signatures of other NK cell subtypes was relatively low. There was no difference in the expression between WT and AD model at different ages. Conversely, the expression of T cell signatures showed a

significant increase in throughout the regions except for the hypothalamus and hippocampus of the AD model compared to the WT mice (**Figure 8D**).

There are still limitations in evaluating the changes of rare cells in spatial distribution through ST analysis. Due to the uncertainty of the marker gene that can specify rare cells and the composition of markers similar to the major brain cell signatures, it is necessary to analyze the results of the current study while considering the limitation of the analysis method through the cell signatures.

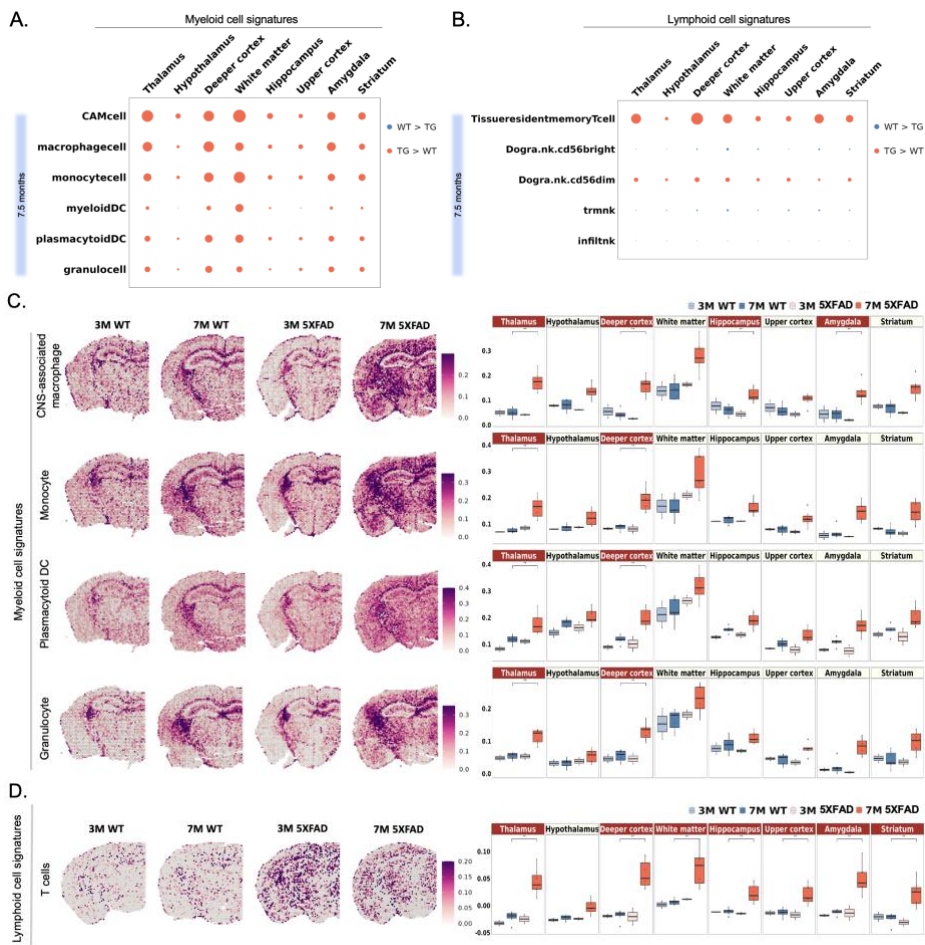


Figure 8. Spatial changes in the distribution of myeloid and lymphoid cell signatures in AD model at different ages

(A) Dot plot showing the average expression differences of various reference-based myeloid cell signatures and (B) lymphoid cell signatures in each region. Expression differences between the three- (left) and 7.5-month-old (right) WT and AD model were indicated. Based on the AD model, the blue dot indicates a decrease, and the red dot indicates an increase. The size of the dots is proportional to the average expression difference value. (C) Spatial pattern of the signatures of CAM, monocyte, plasmacytoid DCs, and granulocyte (left) and the boxplot showing the average expression levels (right). Each dot

represents a mouse in each group. (D) Spatial pattern of the signatures of T cells (left) and the boxplot showing the average expression levels (right). The myeloid cell signatures were increased in the thalamus and deeper cortex of 7.5-month-old AD model compared to the WT, and the T cell signatures were significantly increased throughout the regions except for the hypothalamus region. (7.5-month-old: 7M)

3.1.4.3 Spatial distribution of the subclasses of neuronal signatures in AD model.

As the pathology of AD progresses, aberrant neuronal activity caused by an imbalance of excitatory and inhibitory transmission, and eventual neuronal cell loss occur⁸⁴. To observe neuronal changes in the AD model, I used diverse subclasses of neuronal signatures of excitatory and inhibitory neurons⁸ obtained from single nucleus RNA-sequencing results of the human middle temporal gyrus. Excitatory neuronal subtypes were classified by cortical layers identified with known laminar markers. Inhibitory neurons were first subdivided into large branches of Lamp5, Sncg, Vip, Sst, Pvalb, and Sst Chodl subclasses and further divided according to the expression patterns in each branch. As a result of applying all gene sets of excitatory and inhibitory neuronal subclasses to the ST data, the changes between 7.5-month-old WT and AD model were observed by region (**Figure 9A**). In AD model, the excitatory neuron signatures of L5.6.IT1-subclass showed an increased expression pattern, and the parvalbumin-subclass inhibitory neuronal signature revealed a decreased trend. However, only small changes were observed compared to the changes in genes associated with the most prominently altered subclasses, the somatostatin (Sst)-inhibitory neuron. The expression in the amygdala of AD model only showed a dramatic increase compared to WT, and the expression in other regions showed a tendency to decrease. In particular, the Sst 4-subclass of inhibitory neuron-related genes in the amygdala showed a dramatic increase in AD model at 7.5 months of age (**Figure 9B, C**). Thus, in the early stage of the AD model before accumulation of amyloid plaques, the expression of mature neuron-

related genes was maintained the same as that in age-matched normal mice. However, after accumulation of amyloid plaques in the AD model, a marked increase in specific subclass of inhibitory neuron-associated genes in the amygdala were identified.

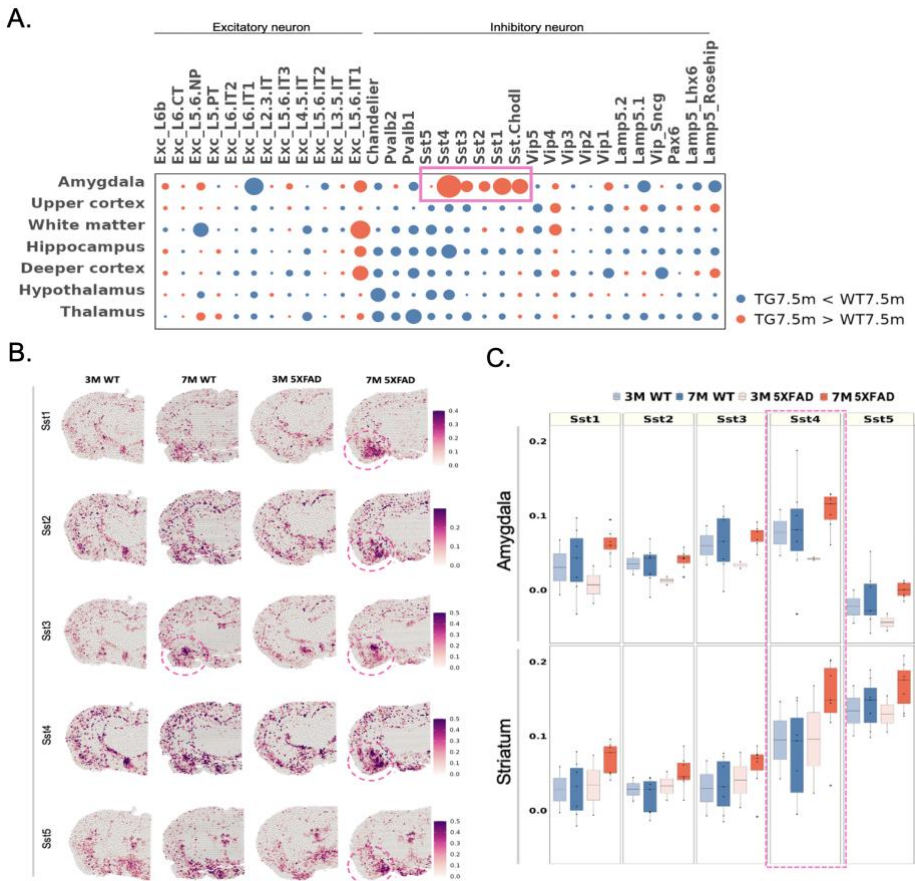


Figure 9. Identification of spatial changes in the distribution of neuronal subclasses in the AD models at different ages.

(A) Dot plot showing the average expression differences of the subclasses of excitatory and inhibitory neurons in eight different regions (hypothalamus, thalamus, hippocampus, deeper cortex, white matter, upper cortex, amygdala, striatum). The average expression differences between the 7.5-month-old WT and AD model are indicated. Based on the AD model, the blue dot indicates a decrease, and the red dot indicates an increase. The size of the dots is proportional to the average expression difference value. The subclasses with the most dramatic changes are indicated by the pink box. (B) Spatial patterns

of somatostatin-subclass of inhibitory neurons that were the most remarkably changed in the AD model compared to the WT mice at 7.5-months-old. The spatial pattern of each brain region was confirmed, and the increased expression pattern was observed exclusively in the amygdala (indicated with pink circles).

(C) The boxplot reveals the average expression level of somatostatin 4-subclass of inhibitory neurons. Each dot represents a mouse in each group. The average expression level in the amygdala showed a tendency to increase in the AD model compared to the WT mice. [#]Bonferroni-adj. p-value was indicated (compared to age-matched WT mice).

3.1.5 Spatial distribution of brain cell state-related signatures in the AD model.

3.1.5.1 Metabolism and senescence-related signatures

Decreased metabolism is one of the most common abnormalities observed in patients with AD. Further, metabolic dysfunction is associated with an inflammatory response, particularly in activated microglia, producing inflammatory factors and shifting metabolism from oxidative phosphorylation (OXPHOS) to glycolysis³⁸. Thus, I observed changes in AD model at three- and 7.5-months using a panel of markers related to OXPHOS and glycolysis (**Figure 10**). The expression pattern of OXPHOS-related genes showed a tendency to decrease in the white matter of AD model compared to WT at both three and 7.5-month-old of age. In contrast, the expression of glycolysis-related genes tended to be increased in the white matter of AD model compared to WT at 7.5-months of age. Notably, most metabolic changes occurred in the white matter, but only a slight change was observed.

Aging is a major risk factor for neurodegenerative diseases, including AD. Under aging or chronic stress, brain cells such as neurons, astrocytes, and microglia can activate cellular senescence mechanisms that promote the functional decline of tissue⁶⁶. In particular, glial cells secreted pro-inflammatory molecules as a senescence-associated secretory phenotype that may induce pathological changes. I used senescence-related markers to identify changes with increasing age and pathological progression in three- and 7.5-month-old WT and AD model. In a comparison between WT mice, the expression of senescence-associated genes slightly increased throughout the

region except for the white matter at 7.5-months compared to three months, but the change was not significant as the age difference was small. Increases were also observed in all regions of 7.5-month-old AD model, with significant changes in the thalamus, deeper cortex, and hippocampus. Thus, senescence-associated genes were observed to be dramatically upregulated in mice with the progression of AD pathologies, including beta-amyloid accumulation and glial cell activation.

Taken together, I characterized spatial and temporal changes in the 5XFAD AD mouse model in the progression of amyloid pathology (**Table 3**). Differential expression analysis of three and 7.5-month-old AD model revealed brain region specifically altered biological pathways. Furthermore, changes in the spatial distribution of various signatures of brain cell subtypes were identified. These results provide useful information for better understanding of amyloid pathology from transcriptomic changes in gross-scale coverage with high spatial resolution.

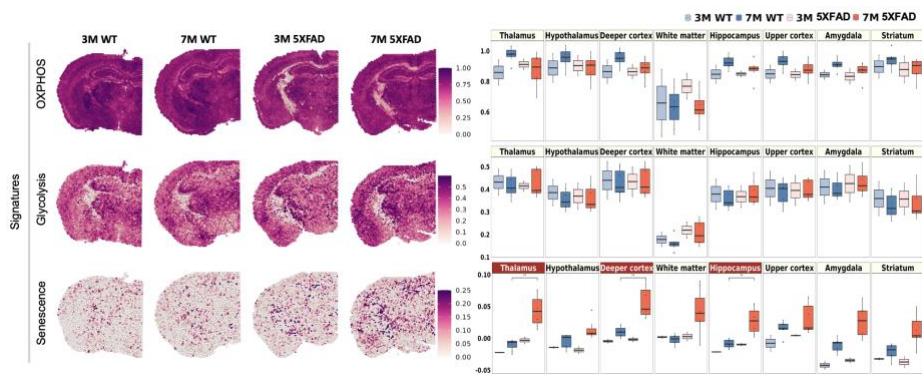


Figure 10. Spatial patterns of the metabolism- and senescence-related signatures in the WT and AD model at different ages.

Spatial patterns of the signatures of oxidative phosphorylation (OXPHOS), glycolysis, and senescence. The representative samples of each group are shown. The boxplots show the average expression levels of the signatures, and groups are displayed in different colors of the boxes. Each dot represents a mouse in each group. The senescence signatures were significantly increased in thalamus, deeper cortex, and hippocampus regions of the 7.5-month-old AD model compared to WT.

| | | 3-month-old 5XFAD model | | 7-month-old 5XFAD model | | | | | |
|---------------------|---|--|--|---|--|-----------------------------------|--|--|--|
| | | Upregulated | Downregulated | Upregulated | Downregulated | | | | |
| Thalamus | Insignificant | Insignificant | Glial cell activation | Mitochondrial function | | | | | |
| Hypothalamus | | | | Neurotransmitter levels | | | | | |
| Cortex | | | | Synaptic function | | | | | |
| Hippocampus | | | | Endoplasmic reticulum stress | | | | | |
| Amygdala | | | | Learning or memory/ Cognition | | | | | |
| Striatum | | | | Protein localization | | | | | |
| White matter | | | | Aerobic respiration | | | | | |
| | | Brain cell signatures | | | | | | | |
| Changes in AD model | | Major brain cells | | | | Rare brain cells | | | |
| Neuron | Microglia | Astrocyte | Oligodendrocyte | Myeloid cells* | Lymphoid cells* | | | | |
| At 3 months | insignificant | Mainly activated microglial signatures showed an increased tendency only in white matter. | Mainly reactive astrocyte signatures showed an increased tendency only in white matter. | insignificant | insignificant | insignificant | | | |
| At 7 months | Increased Sst-inhibitory neuronal signatures in amygdala. | Mainly activated microglial signatures showed increased expression throughout the brain regions. | Mainly reactive astrocyte signatures showed increased expression throughout the brain regions. | Significantly increased in striatum, amygdala, and deeper cortex regions. | Macrophage, monocyte, and dendritic cell signatures showed an increased tendency in white matter, thalamus, and deeper cortex regions. | NK cell signatures: Insignificant | T cell signatures: Increased in thalamus, deeper cortex, and white matter regions. | | |

*Myeloid cells: CAM, macrophages, monocytes, myeloid DCs, plasmacytoid DCs, granulocyte
 *Lymphoid cells: NK cells (tissue resident memory, infiltrating, CD56-bright, CD56-dim), T cells

Table 3. Summary of the spatiotemporal changes in the progression of amyloid pathology.

Summary based on differential expression and brain cell signature analysis of results of applying ST analysis to the 5XFAD AD model at three- and 7.5-months. Brain region-specifically changes genes and cell signatures were identified as the amyloid pathology progressed. (7.5-month-old: 7M)

3.2 Effect of NK cell supplement administration in the 5XFAD AD model

3.2.1 Improvement of behavior function identified via the Y-maze in AD model after administration of NK cell supplements.

Considering that the dramatic increase in glial cell activation was confirmed from the early stage of AD, I used immunotherapeutic agents to confirm the behavior ability improvement effect and demonstrate the feasibility of the ST analysis tool to examine the mode of action. First, I intravenously administrated NK cell supplements to 6.5-month-old AD model and confirmed the improved behavior function (**Figure 11A, B**). The Y-maze behavior analysis revealed an improvement in the NK cell-injected AD model compared to the significantly impaired AD model in the ability to explore new environments. It is necessary to clarify why, where, and how the drugs changed the behavior function for further development as a treatment for AD. Thus, I applied spatial transcriptome to investigate the therapeutic action of NK cell supplements on brain parenchyma by evaluating DEGs and major brain cell signatures in each brain region.

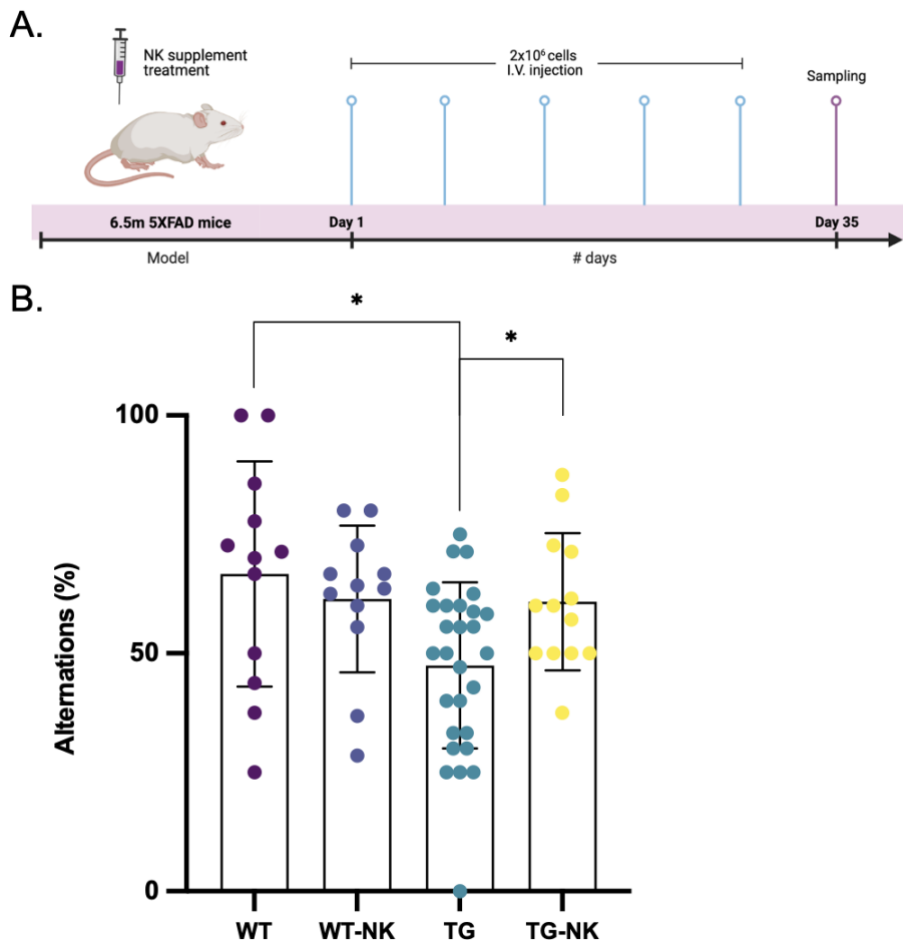


Figure 11. Improved behavior function after NK cell treatment in AD model.

(A) Timeline of the experimental plan for intravenous NK cells administration in 6.5-month-old WT and AD model. After a month, behavior analysis was performed, and samples were obtained for validation. (B) Behavior function of exploring new environments was confirmed using the Y-maze test and expressed as alternating percentages. Each dot represents a mouse in each group. The alternation rate was decreased in the AD model compared to the WT mice, and the recovery of the rate was confirmed after injection of NK cells in the AD model.

3.2.2 Characterization of isolated mouse splenic NK cells.

Isolated NK cells from BALB/c mouse spleen were incubated to amplify the number of cells for seven days prior to characterization and administration. The cells were proliferated and maintained in a healthy condition for seven days (**Figure 12A**). The interferon-gamma (IFN- γ) secretion level from the NK cells was significantly increased after seven days of incubation (**Figure 12B**). Among the sorted cells, 98.71% of cells were NKp46-positive (NK cell), and only a small population of CD3e (T cell; 0.6%)- and CD19 (B cell; 0.6%)-positive cells, which are other immune cell markers, were included (**Figure 12C**). In addition, NKG2D-positive cells harboring the activating immunoreceptor accounted for approximately 65.71% of the total population. The cells in activated status also expressed DNAX accessory molecule-1 (DNAM-1; 65.63%) and CD107a (88.07%) that involve in functional activities such as cytokine secretion. Thus, I demonstrated that approximately two-thirds of sorted NK cells were in an active state and were capable of releasing immunomodulatory cytokines. The composition of isolated NK cells was identified every five injections, and cells under the same conditions were injected into 6.5-month-old WT and AD model.

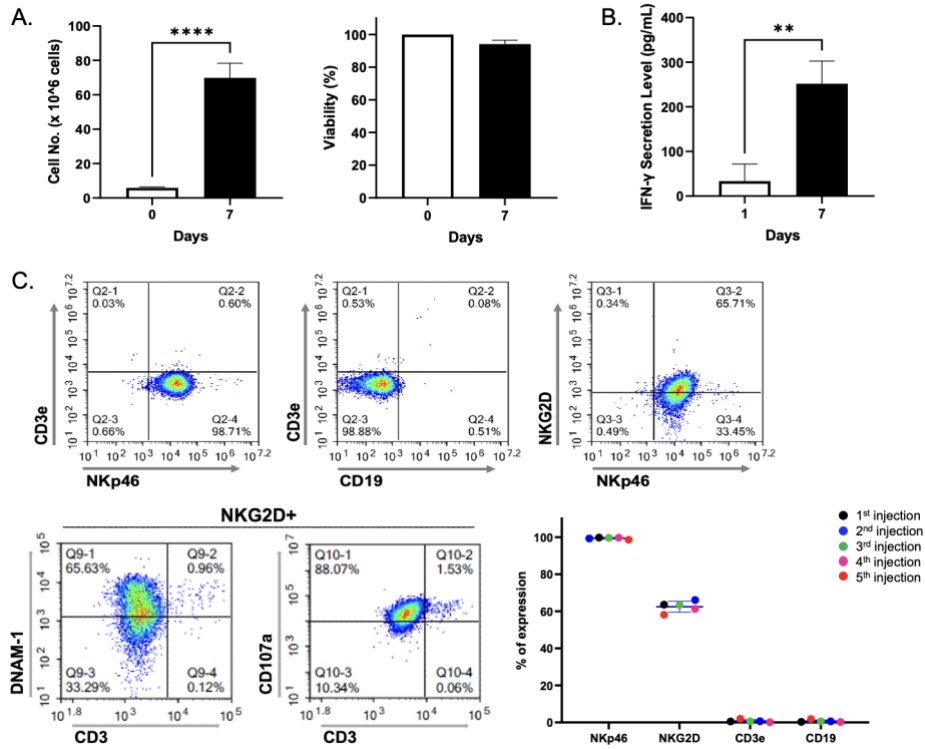


Figure 12. Characterization of isolated mouse splenic NK cells.

(A) Comparison of the NK cell number and viability during NK cell culture on days one and seven. (B) IFN- γ secretion levels on NK cells between days one (33.65 ± 38.12 pg/mL) and seven (251.86 ± 50.58 pg/mL). On day seven, an increase in the level of IFN- γ was confirmed. (C) Flow cytometric analysis of the expanded NK cell population. Expanded NK cells were NKp46 positive (98.71%) and expressed high levels of NKG2D (65.71%), NK activation surface receptor. Moreover, the NK cells contained almost no CD3e (0.53%) and CD19 (0.51%) positive cells. The dots on the cells used for each injection are shown in different colors. Among the NKG2D-positive cells, DNAM-1- and CD107a-positive cells were 65.63% and 88.07%, respectively, and these cells were CD3-negative cells. All mouse NK cells injected five times into mice

showed similar activity and secretion conditions. Data represent the means \pm SD. **p<0.01, ****p<0.0001.

3.2.3 DEGs and related biological pathways after NK cell treatment in the AD model.

Spatial transcriptome data from the brain tissue of NK cell-injected AD model were obtained and compared with the data from saline-injected AD model. First, I investigated the DEGs in NK cell-treated compared to saline-treated AD model in each brain region. The top four regions with the most gene changes were selected as the deeper cortex, white matter, amygdala, and striatum, and the upregulated and downregulated genes were compared (**Figure 13A, B**). In both increased and decreased DEGs in NK cell-injected-AD model, most of the genes in the gray matter regions showed commonly changed genes, whereas a part of the genes in the white matter were region-specifically identified. Genes upregulated in both the gray and white matter included *Lars2*, *mt-Nd3*, *Ftl1*, *mt-Atp8*, *Pttg1*, *Atp5md*, *Pantr1*, *Tmsb10*, *Gm11808*, *mt-Nd4l*, *Ndufa3*, *Gng13*, *Cops9*, *Ndufa5*, *Mt3*, *Cox6c*, *Atp5k*, *Cox7c*, *Atp5mpl*, *Polr2l*, and *Ndufc1*, in order of the fold change values. The downregulated genes included *Gaa*, *Hnrnpdl*, *Sparc*, *Ly86*, *C1qc*, *Ctsd*, *Cirbp*, *C1qb*, *Trf*, *Rbm3*, and *Ftl1-ps1*. The top 20 genes and their associated GO terms in all the major brain regions that were differentially expressed in the NK cell-injected AD model compared to the saline-injected AD model, except for the genes also identified in the NK cell-injected WT mice, are listed in **Table 4**.

Then, I identified the DEGs detected in the white matter region (**Figure 13C**). Genes upregulated in NK cell-injected AD model were associated with functions such as the ATP metabolic process, cellular respiration, oxidative phosphorylation, and aerobic respiration (**Figure 13D**). In addition, functions

related to locomotory behavior and astrocyte differentiation were decreased with increased cellular respiration-related biological pathways in the white matter.

Even in the deeper cortex identified as a representative of the gray matter region, the biological pathways similar to the white matter were altered. DEGs in NK cell-injected compared to saline-injected AD model were identified. The upregulated biological pathways were energy derivation by oxidation of organic compounds, NADH dehydrogenase complex assembly, mitochondrial respiratory chain complex I assembly, and cellular respiration. In contrast, the downregulated pathways were locomotory behavior, glial cell differentiation, astrocyte development, and microglial cell activation. Interestingly, in common with the white matter, an increase in cellular respiration-related genes and a decrease in glial cell differentiation were observed after NK cell treatment in the AD model. Thus, it can be inferred that it shows the overall change pattern of the brain region rather than the exclusive change by region.

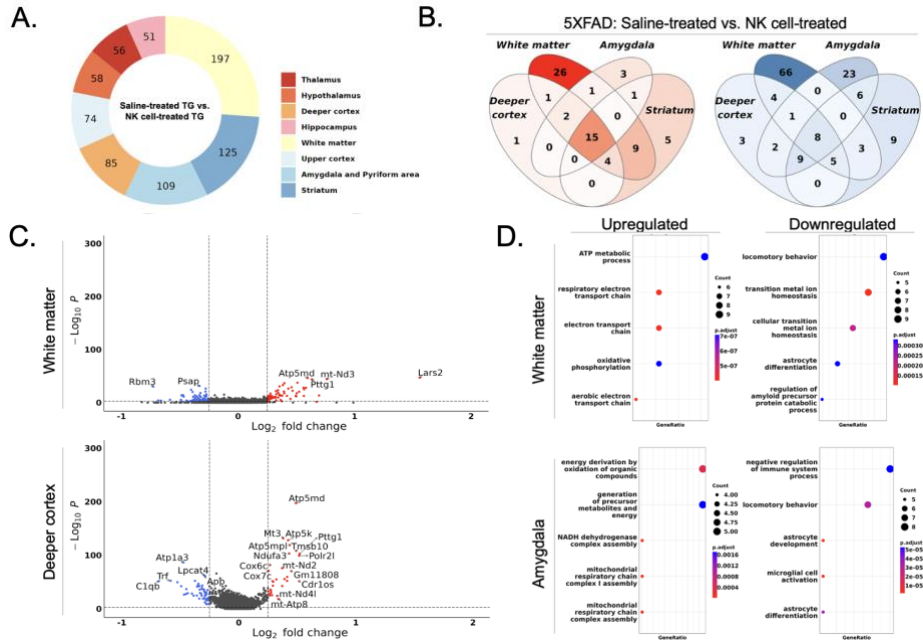


Figure 13. Identification of DEGs and related biological pathways in the NK cell-treated compared to the saline-treated AD model.

(A) Pie chart demonstrating the DEG proportion of NK cell-treated compared to saline-treated AD model in each brain region. (B) Venn diagram representing the upregulated (left; red) and downregulated (right; blue) DEGs in the 7.5-month-old NK cell-treated AD model compared to the AD model. The regions with the most genes are expressed in dark colors. (C) Volcano plot for the genes identified in the 7.5-month-old NK cell-treated AD model compared to the AD model in the white matter and deeper cortex. Genes in the colored dots are significantly (\log_{10} fold change threshold = 0.25) upregulated (red dots) and downregulated (blue dots). The dots colored dark gray represent the genes that are not significantly changed in the NK cell-treated AD model. (D) The top five GO terms related to the upregulated (left) and downregulated (right) genes in the NK cell-treated AD model compared to the AD model in the white matter

and deeper cortex. After NK cell administration, both the white matter and gray matter showed the changes in similar biological pathways. (5XFAD AD model: TG)

Table 4. Representative genes and associated biological pathways that change regionally in NK cell-injected AD model, excluding the changes that occur in WT mice

The top 20 upregulated and downregulated DEGs are listed in order of the fold change values (FDR-adj. p-value < 0.05, logFC threshold = 0.25). The top five GO terms considering the p-value and the number of involved genes are listed. The regions where the related GO pathways were not identified have been left blank.

3.2.4 Biological pathways showing changes after NK cell treatment in AD model.

I identified the altered spatial pattern of glial cell activation- and cellular respiration-related genes after NK cell administration. The signatures of glial cell activation-related pathways were dramatically increased in AD model, mainly in the deeper cortex, white matter, thalamus, and amygdala, compared to WT mice, which show the expression only in the white matter (**Figure 14A**). In AD model treated with NK cells, the expression of the related genes was reduced, and the change was noticeable in the gray matter, while there was no change in the NK cell-treated WT mice. Then, I confirmed the signatures of the cellular respiration-related pathways (**Figure 14B**). Compared to WT mice, the overall expression of AD model tended to decrease, and the change was noticeable in the deeper cortex, thalamus, and striatum. After NK cell administration in AD model, cellular respiratory process-related genes showed increased expression patterns. The inversely changing expression patterns of glial cell activation- and cellular respiration-related genes were identically confirmed in all three experiments.

I identified changes in the expression of individual genes involved in changing biological pathways after NK cell administration. Glial cell activation-related genes that were altered in the NK cell-treated AD model were *B2m*, *Ctss*, *App*, *Gfap*, *Grn*, *Plp1*, *Trem2*, *Vim*, *Agt*, *Bin1*, *Mag*, *Mapk1*, *Tspan2*, *Clu*, *Cnp*, *Enpp2*, *Zfp365*, *Cd9*, *Hexb*, and *Trf*. As the expression level of each gene was different, it was classified into high, medium, and low expression groups (**Figure 14C**). Genes of the low expression group tended to decrease in

most regions of the NK cell-treated AD model. However, the genes in the high and medium expression groups were upregulated in the thalamus, deeper cortex, white matter, and amygdala of AD model in a region-specific manner. Then, a decrease in the corresponding regions was confirmed after NK cell treatment in the AD model. Interestingly, all other genes related to glial cell activation were decreased in the NK cell-injected AD model, but *Trem2*, in contrast, showed an increased expression pattern in the thalamus, deeper cortex, white matter, and amygdala.

Cellular respiration associated genes were *Atp5j2*, *Atp5k*, *Cox5a*, *Cox5b*, *Cox7a2*, *Cox7c*, *Cyce*, *Ndufv3*, *Uqcrb*, *Uqcr10*, *Atp5l*, *Eno1*, *Hspa8*, *Chchd10*, *Ndufa5*, *Cox4l1*, *Ndufb8*, *Uqcrh*, *Mt3*, *Ndufa3*, and *Ndufc1* (**Figure 14D**). All the related genes were downregulated in AD model compared to WT mice. After NK cell treatment in AD model, the expression levels were increased throughout the regions except for in the thalamus. Among all the genes that showed an increasing trend, *Eno1*, *Atp5k*, *Ndufa5*, *Ndufa3*, and *Mt3* showed the highest expression level. In the thalamus of NK cell-treated AD model, only *Atp5k* and *Ndufa3* showed remarkable changes. Taken together, the propensity to reduce glial cell activation and improve metabolic processes according to the therapeutic effect of NK cells was identified at the molecular level, and the regions in which associated genes were expressed were identified.

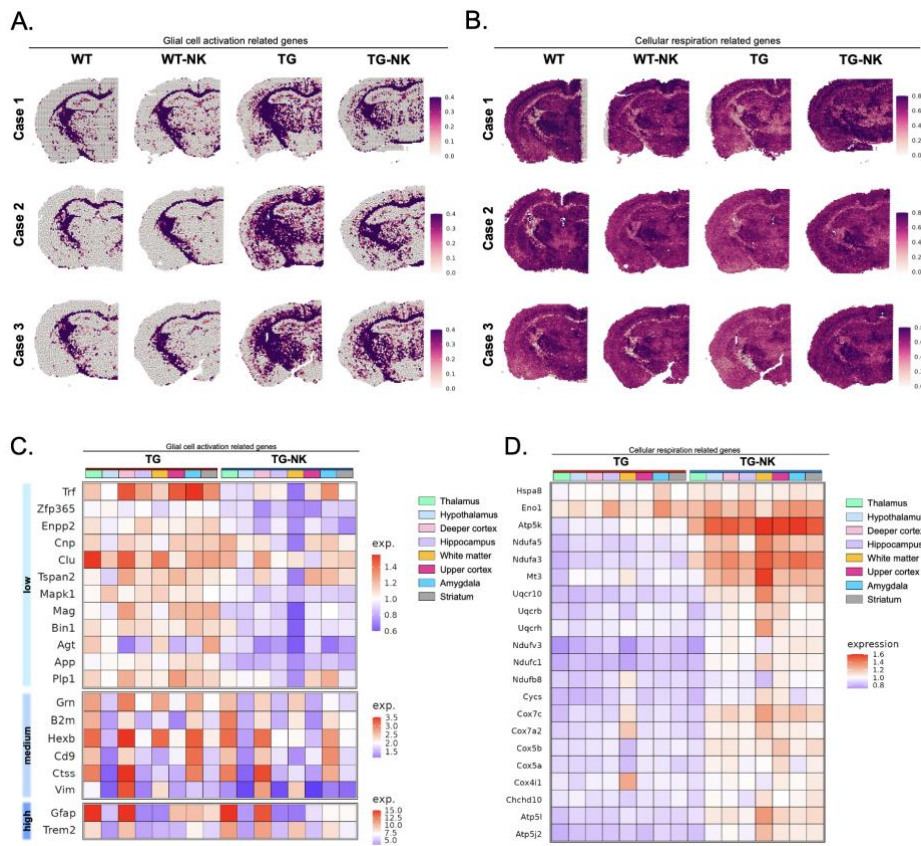


Figure 14. Upregulated and downregulated biological pathways in NK cell-treated AD model.

(A) Spatial pattern of the genes associated with the biological process, glial cell activation, and (B) cellular respiration. In each case, the expression level was compared between the WT, WT-NK, TG, and TG-NK groups. (C) Heatmap of the average expression of individual genes related to glial cell activation and (D) cellular respiration in each region of the TG and TG-NK group. Each region is color-coded, and the relative expression level is also expressed by color. Glial cell activation-related genes were decreased, whereas cellular respiration-related genes showed an increased expression pattern in the TG-NK group compared to the TG group. (5XFAD AD model: TG)

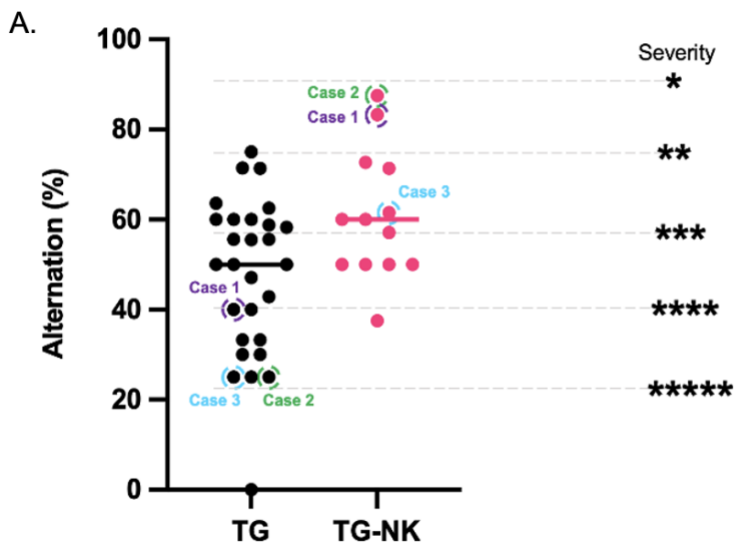
3.2.5 Changed spatial distribution of major brain cells after NK cell treatment in AD model.

The ST data of three cases of NK cell administrated groups were analyzed. The level of behavior ability was indicated for each experimental case and the severity was divided into five stages (**Figure 15A**). Cases were listed from case 1 to 3 in the order of greatest improvement in behavior function after NK cell administration. For case 1, an AD model showing improvement in behavior function with NK cell treatment (severity 1) and an AD model without treatment (severity 5) were compared. For cases 2 and 3, AD model with impaired behavior function (severity 4 and 5) and mice that showed improvement with NK cell treatment at severity levels 1 and 3, respectively, were compared.

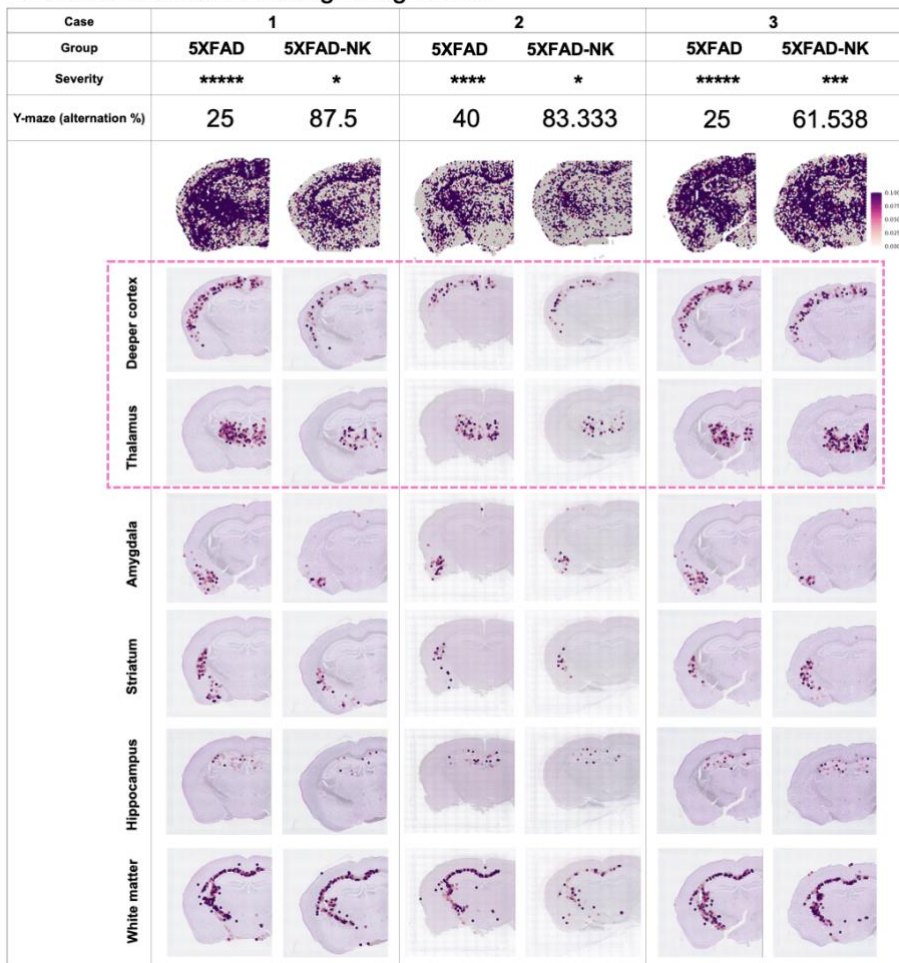
The major brain cell signatures, including microglia, astrocytes, oligodendrocytes, and neurons, were investigated to identify the effect of NK cell treatment on the spatial distribution of brain cells in each case. As a result of examining various brain cell signatures, changes in DAM and somatostatin-inhibitory neuronal signatures were confirmed brain region-specifically in NK cell-treated AD model. First, the spatial expression of DAM signatures was remarkably decreased after NK cell treatment in AD model. The most prominently changed regions were the deeper cortex and thalamus (**Figure 15B**). Interestingly, the difference in the expression of activated microglia in three different cases was proportional to the difference in the improvement of behavior impairment. For instance, the NK cell-injected AD model in case 1 showed a significant improvement in behavior ability and a dramatic decrease

in expression of DAM and plaque-associated microglial signatures compared to the AD model. However, the NK cell-injected mouse in case 3 with a severity 3 of behavior function showed a relatively smaller decrease in the signatures. Depending on the difference in the improvement effect on the behavior dysfunction, there was a variation of the decreased expression level of activated microglia signatures in each case. Thus, the expression of microglial signatures was reduced by the NK cell treatment effect, and in particular, DAM-related genes were decreased mainly in the deeper cortex and thalamus.

The effect of NK cells on neuronal subtypes was evaluated in each brain region using 32 different reference-based excitatory and inhibitory neuronal signatures. Among the subclasses, the somatostatin (Sst)-inhibitory neuron-related genes showed a dramatic decrease in the amygdala region in the AD model after NK cell treatment (**Figure 15C**). The remarkable reduction of Sst-inhibitory neurons was repeatedly confirmed in all three cases, and, in particular, the Sst4-subclass showed the most significant region-specific decrease in the amygdala. The other brain regions showed no definite changes of the neuronal signatures after NK cell treatment. Thus, major brain cell signatures altered by NK cell injection in the AD model were identified brain region-specifically via in-depth analysis using ST.



B.
Disease-associated microglial signatures



C.

Somatostatin inhibitory neuronal signatures

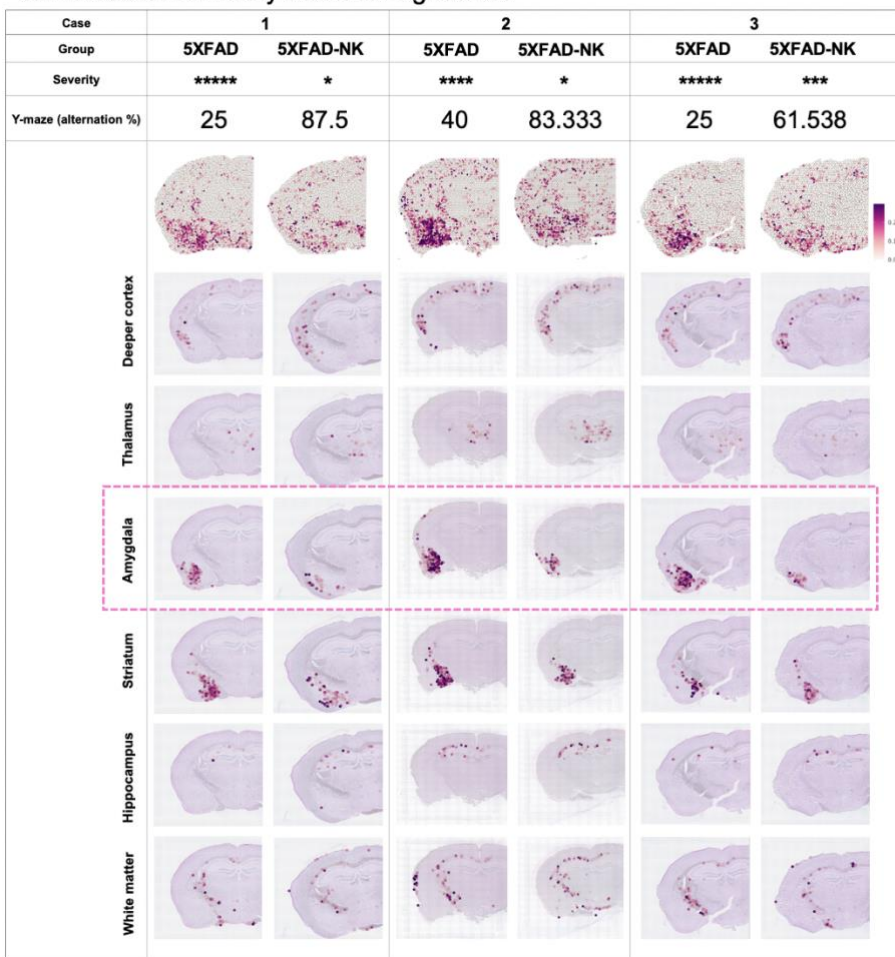


Figure 15. Changes in brain cell signatures after NK cell treatment in AD model.

(A) Result of Y-maze behavior analysis of saline-treated and NK cell-treated AD model. The three cases of mice used for ST analysis were indicated. (B) Spatial pattern of the DAM and (C) somatostatin-inhibitory neuronal signatures in three cases of the experimental groups. The brain images showing the overall expression pattern of the signatures are at the top, and the rest of the images show the expression pattern for each region. Group comparisons are possible

on a case-by-case basis, and the Y-maze results and severity are displayed together. DAM signatures tended to decrease after treatment with NK cells in the AD model, and the changes were remarkable in the deeper cortex and thalamus. Individual differences between cases are large, and it is possible to identify differences in case-by-case comparisons rather than in group comparisons. (5XFAD AD model: TG)

3.2.6 *In vivo* SPECT/CT images and biodistribution of ^{99m}Tc -HMPAO-NK cells.

The biodistribution of ^{99m}Tc -hexamethylpropyleneamineoxime (HMPAO)-labeled NK cells was visualized using SPECT/CT to determine how systemically injected NK cells caused changes in the brain. ^{99m}Tc -HMPAO is well-known for cell labeling as it is a lipophilic radiotracer that is converted to a hydrophilic form by intracellular glutathione and captured inside the cells (**Figure 16A**). After labeling, purification was performed to remove free ^{99m}Tc -HMPAO. The radiochemical purity of ^{99m}Tc -HMPAO-NK cells was 99.5% after the size exclusion column was applied (**Figure 16B**). Then, the purified ^{99m}Tc -HMPAO-NK cells were intravenously injected into normal mice, and the images were acquired by SPECT/CT at 1, 4, and 16 h (**Figure 16C**). Within 1 h after injection, the labeled NK cells were mainly taken up by the liver, and this radioactivity decreased gradually by 16 h. Of note, no definite brain uptake of the labeled NK cells was observed at the resolution of SPECT/CT images. Thus, it was inferred that the administration of NK cells may cause brain changes at transcriptional levels by indirect pathways such as cytokine release or other secretory factors released by altered peripheral immune cells rather than direct effects.

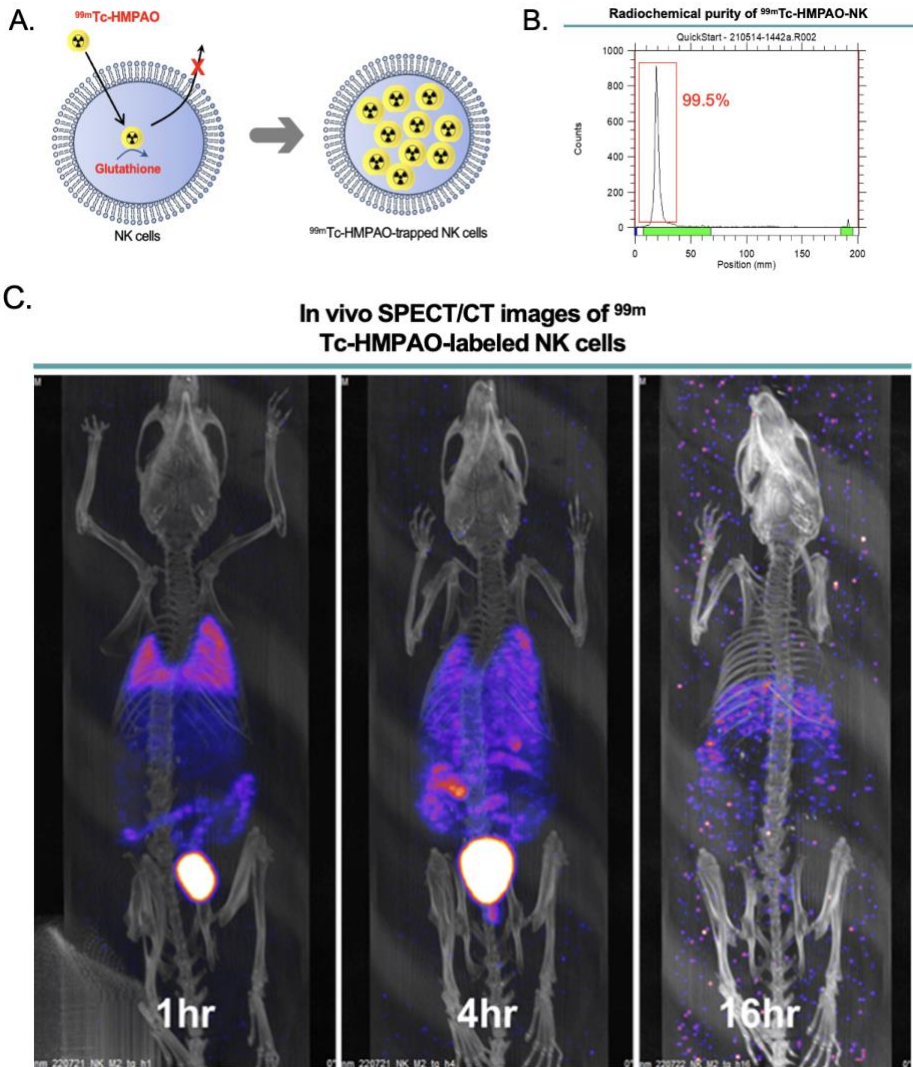


Figure 16. In vivo SPECT/CT images and biodistribution of ^{99m}Tc -HMPAO-NK cells.

(A) Schematic diagram for the radiolabeling method of ^{99m}Tc -HMPAO-trapped NK cells. After highly lipophilic ^{99m}Tc -HMPAO enters the cells, endogenous glutathione in cells begins to convert ^{99m}Tc -HMPAO to a hydrophilic form, which is trapped inside the cells. (B) Radiochemical purification of the ^{99m}Tc -HMPAO-NK cells. The labeled cells were analyzed by instant thin layered

chromatography using Whatman No.1 paper. The radiochemical purification was analyzed right after removing the remaining free ^{99m}Tc -HMPAO. The radiochemical purification was approximately 99.5%. (C) *In vivo* SPECT/CT images of ^{99m}Tc -HMPAO-NK cells injected in mice. After intravenous injection of ^{99m}Tc -HMPAO-NK cells, SPECT/CT images were acquired at 1, 4, and 16 h in C57BL/6 mice. The images showed no significant uptake of the labeled cells in the brain regions.

3.3 Effect of anti-CD4 antibody administration in the 5XFAD AD model

3.3.1 Improvement of behavior function identified via the Y-maze in the AD model injected with anti-CD4 antibody.

For another example of immunotherapeutic agents in the AD model, I intravenously administrated anti-CD4 antibody (aCD4), which also showed improved behavior function analyzed via the Y-maze behavior test (**Figure 17A, B**). After intravenous injection of aCD4, I assessed the altered T cell population in the blood, spleen, deep cervical lymph nodes (dCLN), and brain isolated from the WT and AD model. The blockade of CD4 expression significantly reduced the population of circulating CD4 T cells in the peripheral blood mononuclear cells and spleen (Figure **18A-C**). The CD4 T cell population, which accounts for an average of 60 to 70% of the total T cells, was decreased to an average of 25% after the antibody treatment. The change was equally applied to both WT and AD model. I then analyzed cells in the dCLN, as T cells in the dCLN include cells drained from the brain or meninges via the CSF. The population of CD4 T cells was also significantly reduced in the dCLN after blockade of CD4 expression (Figure **18D**). The proportion of CD4 T cells was the same as in blood and spleen. Then, I identified that systemically altered T cell proportions affected the proportion of T cells present in the brain parenchyma (Figure **18E**). The T cell population among the total brain cells was very small, but I confirmed that the proportion of T cells of the aCD4-injected AD model decreased 2.2-fold compared to the AD model, whereas the

AD model increased 9-fold compared to WT in the hippocampal region. Thus, I confirmed that the CD4 T cell blocking effect was well-maintained after a month of treatment with aCD4 in both WT and AD model. In addition, I determined whether the CD4 blocking effect affected other CD4-positive cells. The surface expression of CD4 was also present on microglia and macrophages⁶⁷. I selected CD11b-positive cells, including both microglia and macrophages, from the cortical region of the brain and analyzed the population of CD4 cells among the cells (**Figure 18F**). The population of CD4-positive cells among the CD11b- and CD45-positive cells was significantly increased in the AD model (approximately 6%) compared to WT (approximately 0.5%). However, there was no difference between before and after treatment with aCD4. Thus, the major change after aCD4 treatment via intravenous injection was a decrease in the population of peripheral CD4 T cells. Then, the ST analysis can be applied to determine how the effect of peripheral CD4 T cell blocking works to improve behavior function.

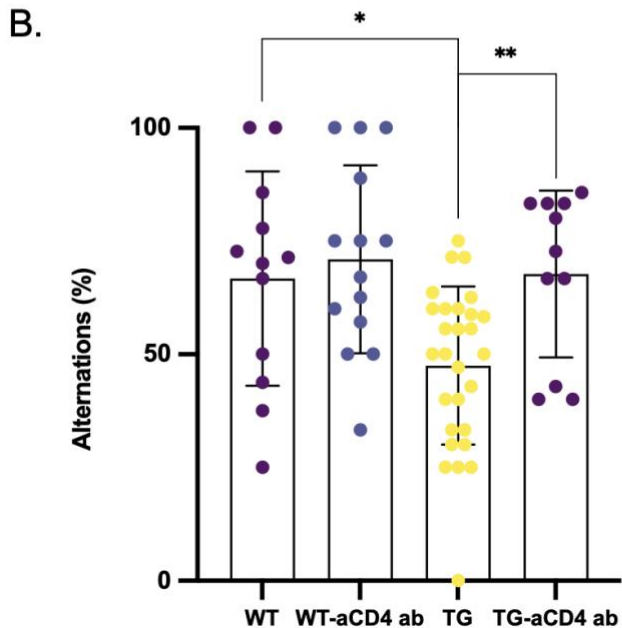
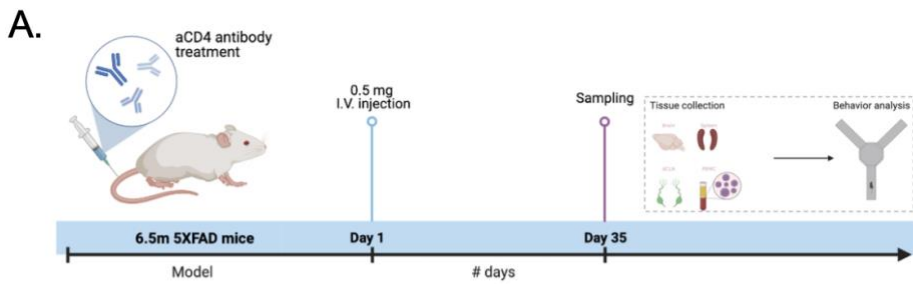
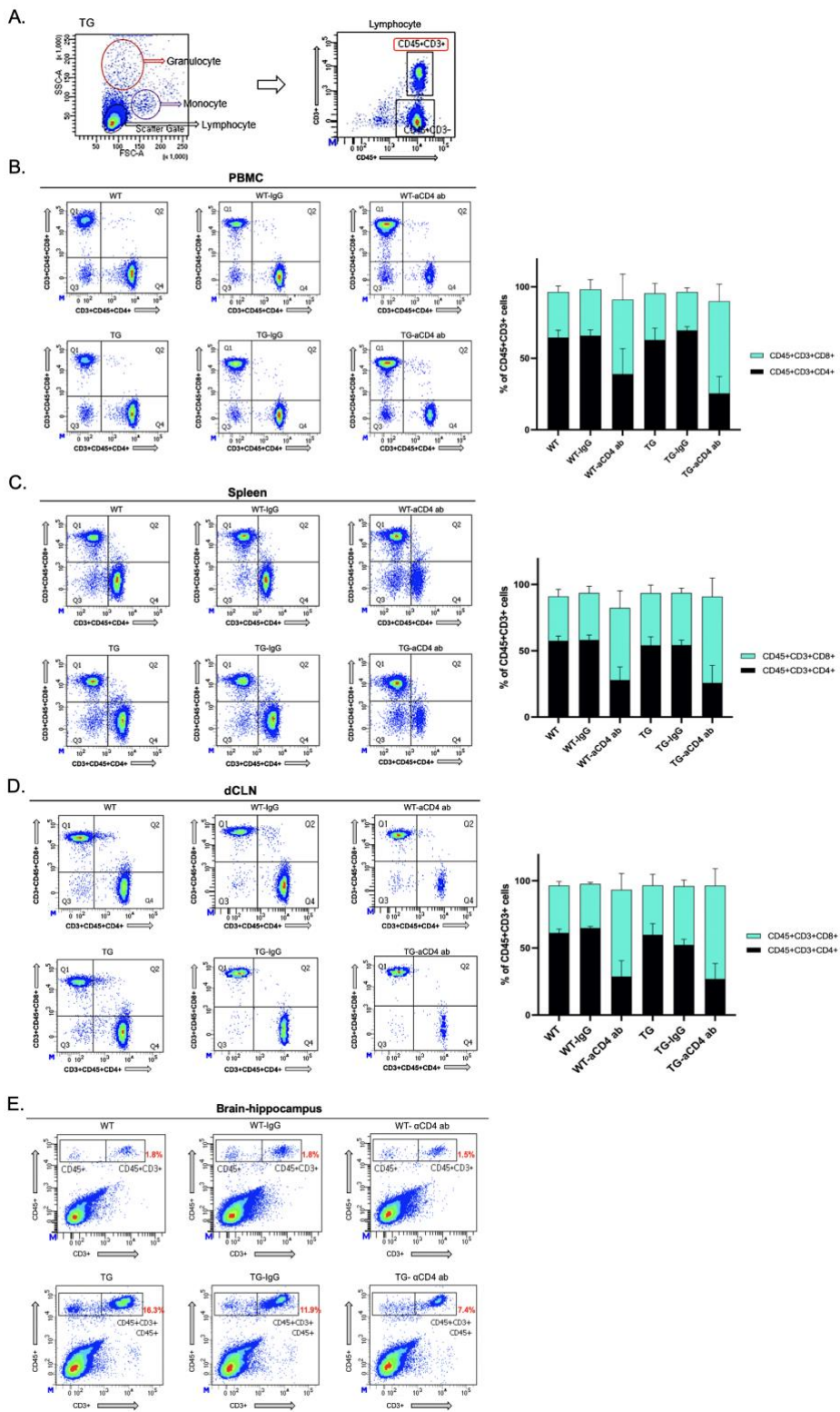


Figure 17. Improved behavior function after anti-CD4 antibody treatment in AD model.

(A) Timeline of the experimental plan for intravenous anti-CD4 antibody administration in 6.5-month-old WT and AD model. After a month, behavior analysis was performed, and samples were obtained for validation. (B) The behavior function of exploring new environments was confirmed using Y-maze and expressed as alternating percentages. Each dot represents a mouse in each group. The alternation rate was decreased in the AD model compared to the WT mice, and the recovery of the rate was confirmed after injection of anti-CD4 antibody in the AD model.



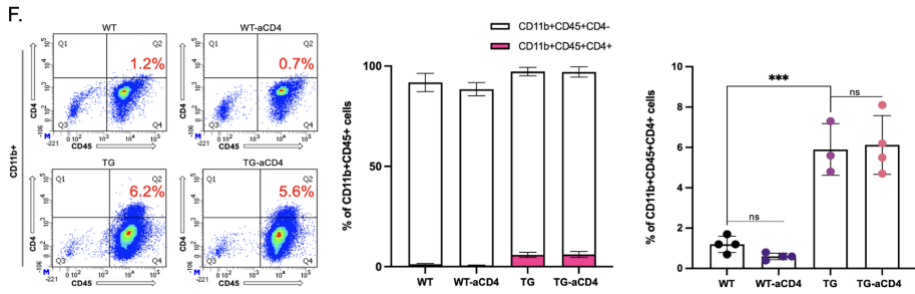


Figure 18. Inactivation of peripheral CD4 T cells in the AD model after anti-CD4 treatment.

After a month of anti-CD4 antibody administration, the changed CD4 T cell population was identified in the blood, spleen, dCLN, and brain. (A) Forward and side scatter plot (FSC vs. SSC) of PBMC on the left and sorted lymphocytes on the right side. The CD45+CD3+ cells indicated by the red box were isolated. (B) Flow cytometry result (left) of the proportion of CD45+CD3+CD8+ and CD4+ cells in the PBMC. The upper row is data from the WT mice, and the lower row is from the AD model. The groups injected with saline, IgG, and anti-CD4-antibodies are in order from left to right. The black bars represent the proportion of CD45+CD3+CD4+ cells, and the blue bars represent the CD45+CD3+CD8+ cells ($n=3$; right). (C) The result shows the CD8 and CD4 T cells in the spleen and (D) dCLN. A significant decrease in the CD45+CD3+CD4+ cells was confirmed in the anti-CD4 antibody injected group in the WT and AD model. (E) Flow cytometry results of the proportion of CD45+CD3+ cells in the brain parenchyma of the hippocampus. Tissues from three mice for groups were combined. The population of CD45+CD3+ cells is shown in the red text. Compared with the WT mice (1.8%), the proportion of T cells increased in the AD model (16.3%) and decreased by

approximately half after the injection of anti-CD4 antibody (7.4%). (F) Flow cytometry results of the proportion of CD11b+CD45+CD4+ cells in the brain. The upper row is data from the WT mice, and the lower row is from the AD model. Groups injected with saline were on the left side, and groups injected with NK cells were on the right side. A bar graph of CD11b+CD45+ cells. The white bar represents the proportion of CD11b+CD45+CD4- cells, and the pink bar represents the CD11b+CD45+CD4+ cells (n=3, 4). The proportions of CD11b+CD45+CD4+ cells are shown for each group. Each dot represents a mouse in each group. Compared to the WT mice, an increase in the CD4 expression was confirmed in the CD11b-positive cells of the AD model, but there was no effect on the proportion of CD11b+CD45+CD4+ cells after anti-CD4 antibody treatment.

3.3.2 Changes in each brain region after anti-CD4 antibody treatment in AD model.

Following the systemic administration of aCD4, I investigated brain region-based alterations at the transcriptional level using ST analysis. First, I compared the upregulated and downregulated DEGs in aCD4-treated compared to none-treated AD model. The DEGs in the white matter, thalamus, hippocampus, and amygdala were compared (**Figure 19A, B**). The highest number of genes was observed in the white matter and most of the genes did not overlap with other brain regions. Only less than 50 DEGs were identified in the gray matter. The top 20 genes and their associated GO terms that were differentially expressed in the aCD4-treated AD model, except for the genes also identified in the aCD4-treated WT mice, are listed in **Table 5**.

Genes upregulated in the white matter of aCD4-treated AD model compared to AD model included *Meg3*, *Snhg11*, *Map2*, *Ewsr1*, *Podxl2*, *Vsnl1*, *Ncdn*, *Stxbp1*, *Tspyl4*, and *Stmn3*, in order of the fold change values (**Figure 19C**). The downregulated genes included *Eif6*, *Sat1*, *Pop5*, *Tmeff2*, *Aprt*, *Psmid14*, *Ctsf*, *Edfl1*, *Clpp*, and *Pslp1*. Then, I identified that the synaptic vesicle cycle and regulation of neurotransmitter levels-related functions were upregulated in the white matter after aCD4 administration (**Figure 19D**). The synaptic function-related genes were *Adcy1*, *Amph*, *Ap3d1*, *Caly*, *Cplx1*, *Cplx2*, *Dnajc6*, *Mapk10*, *Ppp3rl*, *Prkaca*, *Snap25*, *Snap47*, *Snap91*, *Snca*, *Sncb*, *Stxbp1*, *Sv2a*, *Syn1*, *Syn2*, *Syp*, *Trim9*, *Gad2*, and *Slc6a1*. In addition, the biological pathways related to downregulated genes have not been identified. Thus, the only effect after aCD4 treatment in AD model was that the synaptic

function-related genes showed an increased expression exclusively in the white matter, but all the genes showed fold change values of 0.5 or less, resulting in only small changes.

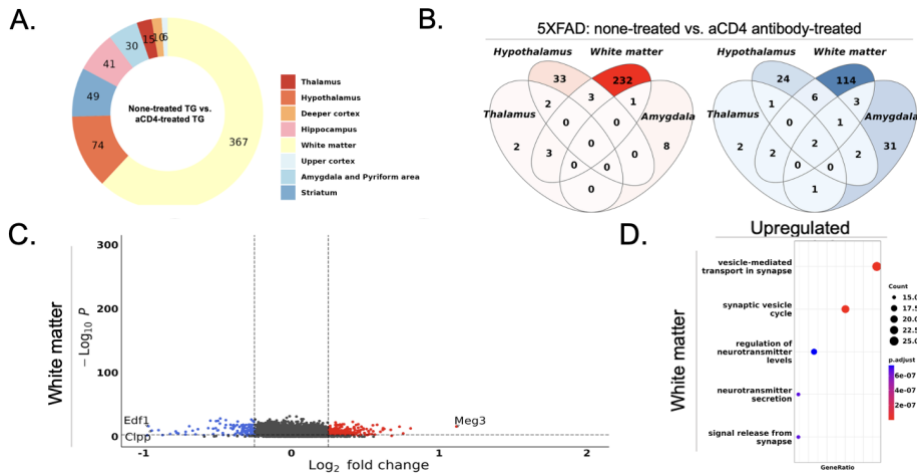


Figure 19. Changes in the white matter of AD model after the administration of anti-CD4 antibody.

(A) Pie chart demonstrating the DEG proportion of anti-CD4-antibody-treated AD model compared to none-treated AD model in each brain region. (B) Venn diagram representing upregulated (left; red) and downregulated (right; blue) DEGs in the AD model injected with anti-CD4 antibody, excluding the DEGs in the WT group. The regions with the most genes are expressed in dark colors.

(C) Volcano plot for the genes identified in the white matter of the AD model injected with anti-CD4 antibody. The genes in the colored dots are significantly (FDR < 0.05 , logFC threshold = 0.25) upregulated (red dots) and downregulated (blue dots). The dots colored dark gray represent the genes that are not significantly changed in the anti-CD4 antibody injected AD model. (D) The top five GO terms related to upregulated genes in the white matter of the AD model injected with anti-CD4 antibody. Notably, genes upregulated in the white matter showed an association with synaptic function, but the fold change level was less than 0.5.

| | | Hypothalamus | Thalamus | Deeper cortex | Hippocampus | White matter | Striatum | Amygdala (Pyriform area) |
|---------------|------|--|--|--|---|---|--|-----------------------------|
| | DEGs | Sted1, Pank, Atpar1, Dsc, Mdp, Gpr1, Mtc, Cyp2, Cyp4, Cyp, Trf, Cox6f1, Sempn2, Cct3, Adoc, Maf, Nidg2, Cab2, Apod, Sis1, Rb2 | Nnat, Hmg, Rgs4, Ctqb, Cplx2, Kif1a, Sted1f | H2-D1, H2-K1, Cat74 | Nnat, Cym, Cnpa7, Gabra2, Nnat, Nnat2 | Meg3, Slc9a7, Meg2, Ewpr1, Pou4f2, Vnnr1, Sgk1, Acvr1, Shabp1, Tap42, Stem3, Nell, Cstz1, Nidg4, Tactd1b, Hmgf, Ocr, Nhlh, Lencf1 | Pigrs, Gabra2, Cym, Dcn, Camta7, Lcn17, Ttr, Nnat, Cyp2, F03nmc4, Bmcc404, Cct3, Igpd1, Dbn, Sh17e7, Gng7, Pcd, Olm7, Piganl2, Uba52, Gabra2, Vnnr1, Cyp | |
| Upregulated | GO | <ul style="list-style-type: none"> Neurotransmitter transport Response to toxic substance Regulation of neurotransmitter levels Neurotransmitter reuptake Neurotransmitter uptake | <ul style="list-style-type: none"> Antigen processing and presentation of peptide antigen Antigen processing and presentation Positive regulation of adaptive immune response Regulation of adaptive immune response Positive regulation of immune effector process | <ul style="list-style-type: none"> Hormone transport O protein-coupled adenine nucleotide transporter activity O protein-coupled purinergic receptor signaling pathway Amyloid precursor protein biosynthetic process Regulation of amyloid precursor protein biosynthetic process | <ul style="list-style-type: none"> Vesicle-mediated transport in synapse Synaptic vesicle cycle Regulation of neurotransmitter levels Neurotransmitter secretion Signal release from synapse | | | |
| Downregulated | DEGs | Apb, Ost, Pmch, Cdc14, Pomp, Npy, Gal, Tubb1, Btr, Horf, Sst, Tac2, Nrb, Sgk1, Lrrk17, Nprv, Vgt, Gpc2, Nrn, Hapt, Gnr10078 | Fgf17-p1, Tubb1, Gnr42418, M2, Gnr10078, Nalubf1-p1, Cdk1ka, Fgf17, Lrrk17, Adc, Cdk1 | Gnr2, Gnr3, Pthrh, Pthrh2, Ven, Tb, Erpp2, Gpr, Egfr3, Lrrk, Hapt1, Nrb2, Sgk1, Tyro3, Arfs, Bdnf, Hornt, Cdk, Chat, Syne1, Lengt | Egr2, Ttr, Pnch, Sft, Pgap6, Tmzf2, Pnch, Bdnf, Vgt, Egfr, Tubb1, Egfr1, Gnr1, Gnr10078, Gndk1, Igpd2, Igpd1, Nmt1, Gnr10078, Fsh, Hornt, Sted1b, Rgs2 | Egr2, Nrb2, Egfr4, Egfr, Rgs2, Pnch, Bdnf, Vgt, Egfr, Tubb1, Egfr1, Gnr1, Tubb3, Apbf1r1g1, Myobp2, Gnr10078, Gndk1, Igpd2, Igpd1, Nmt1, Gnr10078, Fsh, Hornt, Sted1b, Rgs2 | Ttr, Pnch, Gnr10078, Egfr2, Alad, Pnch, Bdnf, Vgt, Egfr, Tubb1, Egfr1, Gnr1, Tubb3, Apbf1r1g1, Myobp2, Gnr10078, Gndk1, Igpd2, Igpd1, Nmt1, Gnr10078, Fsh, Hornt, Sted1b, Rgs2 | |
| Downregulated | GO | <ul style="list-style-type: none"> Neuropeptide signaling pathway Regulation of blood pressure Feeding behavior Positive regulation of blood pressure Penile erection | <ul style="list-style-type: none"> Stress response to metal ion Copper response to zinc ion Opposite inhibition Cellular response to copper ion Nitric oxide mediated signal transduction | <ul style="list-style-type: none"> Regulation of postsynaptic receptor activity Cellular response to copper ion Home biosynthetic process Response to arsenic-containing substance Regulation of adenylate cyclase activity Porphyrin-containing compound biosynthetic process | <ul style="list-style-type: none"> Q protein biosynthesis regulation of cell development Regulation of gliogenesis Olig cell differentiation Positive regulation of gliogenesis | <ul style="list-style-type: none"> Striated muscle tissue development Muscle tissue development Negative regulation of muscle cell differentiation Glycine transport Regulation of anion transmembrane transport | <ul style="list-style-type: none"> Rhythmic process Circadian rhythm Oscillation cycle Circadian behavior Rhythmic behavior | |

Table 5. Representative genes and associated biological pathways that change regionally in anti-CD4 antibody injected AD model, excluding the changes that occur in WT mice

The top 20 upregulated and downregulated DEGs are listed in order of the fold change values (FDR-adj. p-value < 0.05, logFC threshold = 0.25). The top five GO terms considering the p-value and the number of involved genes are listed. The regions where the related GO pathways were not identified have been left blank.

3.3.3 Changed spatial distribution of brain cell signatures after anti-CD4 antibody administration in AD model.

The spatial distribution of major brain cell signatures was observed after aCD4 administration in the AD model. The effects of aCD4 on genes associated with all four cell types (neuron, microglia, astrocytes, and oligodendrocytes) were negligible. The same trend was confirmed in all four cases. Although the signatures of each cell subtype were verified based on various references, the differences between AD model and aCD4-injected AD model were still insignificant. Overall, an increase in synaptic function-related genes was specifically identified in the white matter region after treatment with aCD4 in the AD model, but no change in the spatial distribution of brain cell signatures was observed at the resolution of the ST analysis.

I investigated changes in myeloid and lymphoid cell signatures when treated with aCD4 that improved behavior ability (**Figure 20**). Among myeloid cells, monocyte, plasmacytoid DCs, and granulocyte signatures tended to increase remarkably in the white matter of AD model, but the administration of aCD4 decreased the expression level. In addition, the increased expression level of T cell signatures in thalamus, deeper cortex, white matter, and amygdala was also decreased with the effect of treated aCD4 in AD model. Thus, treatment of AD model with aCD4 resulted the changes in myeloid and T cell signatures rather than the major brain cell signatures. However, as I mentioned above, it is necessary to consider the limitation of ST analysis when evaluating rare brain cell signatures.

Taken together, I applied ST analysis to validate the therapeutic mode of action of NK cell supplements and aCD4 in AD model (**Table 6**). Differential expression analysis of NK cell-treated AD model revealed the increased cellular respiration-related genes and decreased glial cell activation-related genes. Furthermore, the downregulated expression level of DAM signature in the deeper cortex and thalamus and somatostatin-inhibitory neuronal signature in the amygdala were identified. After aCD4 treatment in AD model, synaptic function-related genes were upregulated, and the expression level of myeloid and T cell signatures were downregulated exclusively in the white matter. Thus, I demonstrated the applicability of evaluating AD therapeutics to explain behavioral improvement via brain region-based in-depth analysis.

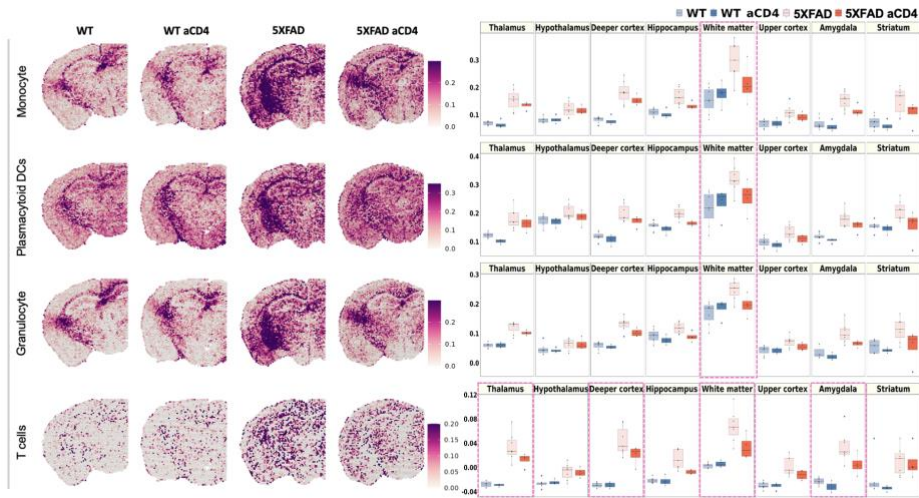


Figure 20. Changes in brain cell signatures after anti-CD4 antibody treatment in AD model.

Spatial patterns of the signatures of myeloid and lymphoid cells including monocyte, plasmacytoid DCs, granulocyte, and T cells. The representative samples of each group are shown. The boxplots show the average expression levels of the signatures, and groups are displayed in different colors of the boxes. Each dot represents a mouse in each group. The regions showing a decreased tendency after anti-CD4 antibody treatment were indicated with pink boxes. The myeloid and T cell signatures tended to decrease in the white matter region with the effect of anti-CD4 antibody in AD model.

| Changes in AD model | Treatment | | Differentially expressed genes | | | |
|-----------------------|--|---|---|----------------------|--|---|
| | Characteristics | Effect after a month | Regions | Upregulated | Downregulated | |
| aCD4 | <ul style="list-style-type: none"> i.v injection Clone: GK1.5 | Blocking CD4 T cells | White matter | Synaptic function | - | |
| NK cell | <ul style="list-style-type: none"> i.v injection Isolated from mouse spleen Most NK cells containing activating receptors | - | All regions | Cellular respiration | Glial cell activation | |
| Brain cell signatures | | | | | | |
| Changes in AD model | Major brain cells | | | | Rare brain cells | |
| | Neuron | Microglia | Astrocyte | Oligodendrocyte | Myeloid cells* | Lymphoid cells# |
| aCD4 | insignificant | insignificant | insignificant | insignificant | Monocyte, plasmacytoid DCs, granulocyte signatures : A slight decrease in white matter | T cell signatures: A slight decrease in white matter and amygdala |
| NK cell | Decreased Sst-inhibitory neuronal signatures in amygdala | Decreased DAM and plaque-associated microglial signatures in deeper cortex and thalamus | Decreased reactive astrocyte signatures in deeper cortex and thalamus, but only with dramatic cognitive improvement | insignificant | insignificant | insignificant |

*Myeloid cells: CAM, macrophages, monocytes, myeloid DCs, plasmacytoid DCs, granulocyte
 #Lymphoid cells: NK cells (tissue resident memory, infiltrating, CD56-bright, CD56-dim), T cells

Table 6. Summary of the feasibility test of ST analysis for verifying the mode of action of AD therapeutics in AD model.

Summary based on differential expression and brain cell signature analysis of results of applying ST analysis to the 5XFAD AD model after administration of NK cells and anti-CD4 antibody. The changes in genes and cell signatures were identified as the mode of action of therapeutic agents that exhibit behavior improvement.

4. Discussion

Although studies have assessed the pathological progression of AD, there is still a need to understand the regional differences of AD in the brain. Spatial transcriptomics was selected as the method of the year 2020 by Nature Methods²⁰ and was evaluated for its high utility in the search for biological meanings. I applied brain tissues from AD mouse models to spatial transcriptome analysis, which is appropriate for analysis considering spatial heterogeneity. The brain regions were well defined according to anatomical structures through unsupervised clustering without other segmentation techniques (**Figure 2B**). Even the border region or ventricular area, which occupies only a small portion of the coronal section I obtained, was distinguished. There are approximately 4,000 to 8,000 spots in each cluster subdivided into the white matter and gray matter regions, which is suitable for finding meaningful results (**Figure 2E**). I established a thorough analysis procedure by integrating two methods. First, I set a region of interest in the brain to find the changing genes. Second, I set a gene combination and identified where it is located (**Figure 1**). This workflow was applied to identify changes according to the pathological progression of AD and to verify the therapeutic effects.

First, the transcriptional changes in each brain region according to the pathological progression of AD were identified by comparing AD models before and after definite accumulation of amyloid plaques. An interesting biological finding in the present study is the initial changes in the white matter

prior to the distinct changes in the gray matter in AD models (**Figure 3**). AD has been considered a gray matter disorder, but recently, abnormalities in the white matter, including demyelination and degeneration, have been attracting attention as an important pathophysiological feature⁶⁸. The results of the current study showed that DEGs increased in the white matter of the three-month-old AD model before definite amyloid deposition were associated with gliogenesis (**Figure 4A-C**). Among the increased genes exclusively found in the white matter, *Mag* is known to be an inhibitor of axonal sprouting⁶⁹, which is critical for synapse formation. A decrease in synapse organization-related biological pathways was confirmed in the white matter of the three-month AD model. It can be inferred that the aberrant alterations in the expression of specific genes mainly involved in gliogenesis in the white matter affect synapse loss before pronounced amyloid accumulation.

With the progression of AD pathology, glial cell activation-related genes were dramatically increased in both the white and gray matter with severe amyloid deposition. Notably, most genes that increased at 7.5 months differed from those identified at three months (**Figure 4D-F**). The only gene commonly expressed is *Gfap*, which is known to reflect memory decline and white matter health independently of beta-amyloid or tau protein⁷⁰. Upregulated genes associated with reactive glial cells in both the white and gray matter in the 7.5-month-old AD model included *Trem2*, *Tyrobp*, and *Cst7*. These genes are known AD risk factors and are also included in DAM-related genes⁴³. In particular, the triggering receptor expressed in myeloid cells 2 (*Trem2*) is an essential gene for activation into DAM. Thus, in the AD model, changes in

genes independent of amyloid plaques appear at first, and, as the pathology of AD progresses, an increase in *Trem2*-dependent inflammatory signals is sequentially confirmed. In addition, the association of increased genes in the thalamus of AD model with the antigen presentation pathway has been shown, and *Trem2* is also involved. In particular, microglia may represent the main antigen-presenting cells in the brain parenchyma, and the involvement of infiltrated immune cells may function in AD pathological progression⁷¹. Thus, an association of adaptive immunity with prominent amyloid plaque deposition in the gray matter was inferred.

I analyzed diverse brain cell signatures to characterize the spatial distribution of each cell type in the AD model. In particular, the signatures of microglia, ARP, macrophages, and monocytes showed an upregulated expression level in AD model compared to WT, and each cell signature showed a region-specific expression distribution (**Figure 6A, B**). For instance, the signatures of microglia and macrophages showed a dramatic increase in the gray matter, where amyloid deposition is mainly presented, whereas ARP showed a more intense increase in the white matter. Among the subtypes of glial cells, the signatures of DAM showed remarkable increases in the white matter of early AD, which is consistent with the finding of the initially altered DEGs in the three-month AD model (**Figure 7A, B**). A recent report characterized white matter-associated microglia (WAMs), which share parts of the signatures of DAM, but are more aging dependent and engaged in clearing myelin debris⁷². WAM appeared in three-month-old *APP^{NL-G-F}* mice, which could reveal that myelin degeneration starts earlier than amyloid pathology.

Like microglia, the signature of reactive astrocytes showed the same activation patterns, initially starting from the white matter to the thalamus and cortex area (**Figure 7C, D**). The spatial distribution of reactive astrocyte signatures revealed a correlation with the signature of white matter associated astrocytes rather than gray matter associated. However, the subtypes of oligodendrocytes were not involved in the early change in the white matter of the AD model (**Figure 7E, F**). In summary, the white-to-gray matter transition provides important information about the pathological changes in AD progression, but further studies are needed to determine whether this transition occurs independently and how glial cells communicate in each brain region.

Alteration of rare immune cells in each brain region in the AD model was also estimated (**Figure 8**). Compared to normal mice, in the AD model, the signatures of myeloid cells and T cells were increased throughout the regions. These results are consistent with the reports that the infiltration of peripheral immune cells into the brain parenchyma has been identified in the AD model, and the crosstalk contributes to the neuroinflammatory response of pathology. However, it is necessary to recognize that there are still technical limitations to studying rare immune cells with ST analysis. It is unclear which genes specifically define rare cells, and markers overlap with major brain cells such as microglia or astrocytes. Thus, the development of technical complements for a spot-based analysis of rare cells is essential, and only inferences are possible with the current results.

In the 7.5-month-old AD model, the top five upregulated biological pathways were mainly associated with glial cell activation across regions,

whereas the downregulated genes related functions differed in each region (**Figure 5**). In particular, a decrease in oxidative phosphorylation-related genes in the white matter proceeded along with an increase in the abnormal activity of glial cells, which was confirmed using a gene combination of oxidative phosphorylation signatures (**Figure 10**). The reduction of oxidative phosphorylation in the white matter was remarkable compared to other regions. Accumulated amyloid plaques in the 7.5-month-old AD model may have directly triggered microglial activation by reprogramming their metabolic pathways toward aerobic glycolysis³⁸, which may also occur in reactive astrocytes⁷³. The data presented here may help understand AD further and facilitate the discovery of targeted therapeutics by providing extensive information on regions with different pathological characteristics of AD.

I evaluated the changes in neuronal signatures in the AD model showing amyloid pathology. First, mature neuronal signatures were decreased in the WT and AD model at 7.5 months compared to at three months of age (**Figure 9**). Then, I determined the changed balance between excitatory and inhibitory neurons by subdividing the neuronal subclasses in the 7.5-month-old WT and AD model. Among the 32 subclasses of excitatory and inhibitory neuronal signatures, somatostatin (Sst)-inhibitory neuron-related genes were remarkably increased in the amygdala. Sst is a well-known neuropeptide expressed throughout the brain, and the functional roles of Sst-inhibitory neurons were studied mostly in the cortex⁷⁴. Neurons expressing Sst in the cortex contribute to modulating cortical circuits, particularly excitatory inputs to the sensory cortex, and are also known to be involved in synaptic plasticity. Most

importantly, Sst-inhibitory neurons are known to play an important role in maintaining spatial working memory. The reduced expression of Sst is a hallmark of various neurological disorders. For instance, patients with AD exhibited low Sst expression in the cortex and hippocampus⁷⁵. As Sst enhances the enzyme activity of neprilysin, which promotes beta-amyloid degradation⁷⁶, disruption of Sst function may affect the progression of AD. However, the function of Sst-inhibitory neurons in the amygdala remains poorly understood.

The importance of understanding amygdala abnormalities seen in AD has been emerging. Amygdala atrophy was confirmed using structural magnetic resonance imaging to be comparable to hippocampal atrophy in patients with mild AD^{77,78}. In addition, the relationship of amygdala atrophy to global behavior functioning, and predicting AD progression is considered possible using the atrophy state. Thus, increased Sst-inhibitory neuronal signatures in the amygdala are expected to be important for understanding AD pathology, and further studies are required.

In the ST analysis of the AD models of different ages, the increase in glial cell activation-related genes was prominent as the AD progressed. As it has been revealed that peripheral immune cells, including monocytes, neutrophils, NK cells, T cells, and B cells, can contribute to neuroinflammation in neurodegenerative disease⁷⁹, the development of therapeutic agents to control them is underway. However, since AD is a complex and multifactorial disease, the validation of therapeutic agents should be reviewed from various perspectives. Thus, I applied ST analysis to identify the feasibility of the method to investigate the therapeutic effects. Here, I applied NK cell

supplements and aCD4 as AD therapeutic agents as these showed an improvement in spatial memory function in the Y-maze behavior analysis of the AD model (**Figure 11, 17**).

NK cells in active status release diverse cytokines and modulate immune response. Patients with AD have a significantly lower functional potential of NK cells compared to normal controls⁸⁰. However, the role of NK cells in AD is still controversial⁸¹, and a more detailed investigation at the transcriptional level is required. I used NK cells isolated from the spleen of mice, and the characteristics of the cells were identified. Two-thirds of the isolated NK cells were active (**Figure 12**), containing activating receptors on their surface and capable of secreting immunomodulatory cytokines. Application of the ST analysis showed that the administration of NK cells attenuated the upregulation level of glial cell activation-related genes in the AD model (**Figure 13**). Reactive glial cell markers that were increased in the 7.5-month-old AD model, such as *Gfap*, *Vim*, *Ctss*, and *Cd9*, were decreased after NK cell administration. Interestingly, the genes that showed an early increase in the white matter at three months in the AD model, such as *Mag*, *Bin*, and *Plp1*, were also decreased by NK cell administration. This indicates that even the abnormally increased genes related to gliogenesis seen in early AD were normalized by the effect of NK cells in the AD model. While genes related to glial cell activity were downregulated throughout brain regions, cellular respiration-related genes were upregulated mainly in the deeper cortex, thalamus, and striatum after NK cell treatment (**Figure 14**). Reduced expression of proteins involved in oxidative phosphorylation pathways in patients with AD has been confirmed in the

cortical region of the brain⁸². In addition, the expression level of *Atp5k*, which is ATP synthase, and *Ndufa3*, which is involved in mitochondrial respiratory chain complex assembly, showed a marked increase throughout regions. This result may infer the recovery of mitochondrial dysfunction, one of the pathological hallmarks of AD. Thus, restoration of cellular respiration function following NK cell injection may be closely related to improved behavior function.

NK cell administration affected the microglial signatures rather than astrocytes and oligodendrocytes signatures (**Figure 15**). Decreased signatures of DAM were particularly pronounced in the deeper cortex and thalamus, consistent with regions with an increased expression of cellular respiration-related genes. Notably, the expression of DAM signatures tended to decrease the most when the behavior ability was most improved. Therefore, the correlation between the severity of behavior function and the expression level of activated microglial signatures can be expected.

The expression of Sst-inhibitory neuronal signatures in the amygdala, which was aberrantly increased in the AD model, was decreased to a normal level after NK cell treatment. Normalization of excitatory and inhibitory neuronal imbalances in the amygdala of the AD model may improve behavior function. Detailed investigation of the neurons in the amygdala region could play an important role in understanding the pathology of AD and in providing therapeutic directions.

Since the infiltration of injected NK cells into the brain was not observed at the SPECT/CT image resolution (**Figure 16**), it is necessary to consider the

effects of released cytokines or changed peripheral immune cells by NK cell administration. It is known that IFN-gamma, which is known to be released by activated NK cells, induces phagocytosis of cerebral beta-amyloid in AD by restoring microglia autophagy and eventually improves cognition in APP/PS1 mice^{36,83}. IFN-gamma plays a critical role in metabolic reprogramming between oxidative phosphorylation and glycolysis to restore the phagocytic activity of tolerant microglia³⁸. Moreover, GM-CSF is also released from NK cells and may be a candidate for therapeutic effects in AD. Of note, GM-CSF treatment revealed safe and memory-enhancing benefits to patients with AD and is currently being studied in a phase II clinical trial⁸⁴. Even if the infiltration of intravenously injected NK cells into the brain parenchyma was not identified in the SPECT/CT image resolution, it is difficult to rule out the possibility. However, considering that there was not sufficient cell infiltration as seen in SPECT/CT images, it is possible to infer the effect of immunomodulatory cytokines released from injected NK cells on the improvement of the behavior function shown in the AD model.

As another example of an AD therapeutic to evaluate the applicability of ST analysis to identify the mode of action, I evaluated the therapeutic efficacy of aCD4 in the AD model. The imbalance between effector T cells and regulatory T cells accelerated memory impairment and neuroinflammation⁸⁵. In detail, misfolded proteins may drain into peripheral lymphoid tissue and be presented to naïve T cells. Particularly, Th1 and Th17 CD4 T cells may directly or indirectly activate microglia and astrocytes to affect neuronal cell death. In patients with AD and mild cognitive impairment compared to healthy

individuals, beta-amyloid-specific naive and central memory CD4 T lymphocytes were decreased, and Th17 and Th9 CD4 T cells were increased⁸⁶. The aCD4 was intravenously administrated in the AD model and confirmed improvement in behavior function after a month. The blocking effect of peripheral CD4 T cells was demonstrated (**Figure 18**), and, interestingly, the T cell population in the hippocampal area of the brain was decreased after aCD4 treatment. However, there was no change in the CD4-expressing microglia and macrophage population, which were significantly increased in the AD model compared to age-matched WT mice. Thus, ST analysis was performed to determine by what action aCD4 treatment, which mainly affects changes in the CD4 T cell population, affects behavior function improvement.

After aCD4 administration in the AD model, genes were predominately changed in the white matter region and synaptic function-related genes were upregulated, but only with slight changes (**Figure 19**). While changes in the major brain cell signatures were also insignificant, the administration of aCD4 resulted in decreased expression levels of myeloid cells and T cell signatures in the white matter region of the AD model (**Figure 20**). Given the increased synaptic function in the white matter region after aCD4 treatment, this may be associated with the decrease in the peripheral immune cell signatures. However, it is necessary to consider that evaluating rare brain cell signatures has technical limitations. Thus, both NK cell and aCD4 treatment in AD model showed the behavior improvement analyzed via Y-maze, but the target brain regions and the mode of mechanisms were different.

Taken together, I identified the genes and cell signatures changed by the effect of AD therapeutics based on the understanding of amyloid pathology from transcriptomic changes in each brain region. More on that, the ST analysis results are important in that it is possible to identify the genes that are not changes by drugs and to identify the target site where the drug works. Since the introduction of a drug efficacy evaluation method considering spatial heterogeneity of the brain is essential, ST can be applied to a comprehensive analysis of AD therapeutics. For further study, it is important to increase penetration into the brain to maximize the efficacy of the treatments I used. As one method, NK cell-derived exosomes could be used for therapeutic agents. Exosomes containing proteins and RNA derived from donor cells act as communicators between cells⁸⁷. Furthermore, the attractive advantage is that it can cross the BBB and affect the brain. The immunomodulatory ability of extracellular vesicles from mesenchymal stromal cells has been demonstrated⁸⁸. Moreover, I can deliver the isolated exosomes from NK cells or aCD4 by intrathecal injection rather than systemic injection. That way, the drugs can reach the ventricular region directly and be mixed with CSF⁸⁹. Thus, it would be possible to increase the therapeutic effect by achieving the global distribution of drugs to the CNS.

5. Conclusion

The results of the current study provide resources for the progression of AD pathology-related transcriptomic changes in gross-scale coverage with high spatial resolution. As it appears that cellular changes in a small region of the brain cannot represent changes in the whole brain, the results presented here may provide a new basis for understanding AD. In addition, I demonstrated the feasibility of validating the effectiveness of AD therapeutics via an in-depth analysis of the complex nature of AD pathology. Overall, I hope that this approach can help researchers to interpret real action of drug candidate by simultaneously investigating the dynamics of all transcripts for the part of development of novel AD therapeutics.

6. References

- 1 Manzoni, C. *et al.* Genome, transcriptome and proteome: the rise of omics data and their integration in biomedical sciences. *Brief Bioinform* **19**, 286-302, doi:10.1093/bib/bbw114 (2018).
- 2 Szabo, P. A. *et al.* Single-cell transcriptomics of human T cells reveals tissue and activation signatures in health and disease. *Nature Communications* **10**, 4706, doi:10.1038/s41467-019-12464-3 (2019).
- 3 Li, C., Guo, L., Li, S. & Hua, K. Single-cell transcriptomics reveals the landscape of intra-tumoral heterogeneity and transcriptional activities of ECs in CC. *Mol Ther Nucleic Acids* **24**, 682-694, doi:10.1016/j.omtn.2021.03.017 (2021).
- 4 Ximerakis, M. *et al.* Single-cell transcriptomic profiling of the aging mouse brain. *Nat Neurosci* **22**, 1696-1708, doi:10.1038/s41593-019-0491-3 (2019).
- 5 Van Hove, H. *et al.* A single-cell atlas of mouse brain macrophages reveals unique transcriptional identities shaped by ontogeny and tissue environment. *Nat Neurosci* **22**, 1021-1035, doi:10.1038/s41593-019-0393-4 (2019).
- 6 Mathys, H. *et al.* Single-cell transcriptomic analysis of Alzheimer's disease. *Nature* **570**, 332-337, doi:10.1038/s41586-019-1195-2 (2019).
- 7 Yao, Z. *et al.* A taxonomy of transcriptomic cell types across the isocortex and hippocampal formation. *Cell* **184**, 3222-3241.e3226, doi:10.1016/j.cell.2021.04.021 (2021).
- 8 Hodge, R. D. *et al.* Conserved cell types with divergent features in human versus mouse cortex. *Nature* **573**, 61-68, doi:10.1038/s41586-019-1506-7 (2019).
- 9 Pöyhönen, S., Er, S., Domanskyi, A. & Airavaara, M. Effects of Neurotrophic Factors in Glial Cells in the Central Nervous System: Expression and Properties in Neurodegeneration and Injury. *Front Physiol* **10**, 486, doi:10.3389/fphys.2019.00486 (2019).
- 10 Matias, I., Morgado, J. & Gomes, F. C. A. Astrocyte Heterogeneity: Impact to Brain Aging and Disease. *Front Aging Neurosci* **11**, 59, doi:10.3389/fnagi.2019.00059 (2019).
- 11 Batiuk, M. Y. *et al.* Identification of region-specific astrocyte subtypes at single cell resolution. *Nat Commun* **11**, 1220, doi:10.1038/s41467-019-14198-8 (2020).
- 12 Floriddia, E. M. *et al.* Distinct oligodendrocyte populations have spatial preference and different responses to spinal cord injury. *Nat Commun* **11**, 5860, doi:10.1038/s41467-020-19453-x (2020).
- 13 Marques, S. *et al.* Oligodendrocyte heterogeneity in the mouse juvenile and adult central nervous system. *Science* **352**, 1326-1329, doi:10.1126/science.aaf6463 (2016).
- 14 Masuda, T. *et al.* Spatial and temporal heterogeneity of mouse and human microglia at single-cell resolution. *Nature* **566**, 388-392, doi:10.1038/s41586-019-0924-x (2019).

- 15 Olah, M. *et al.* Single cell RNA sequencing of human microglia uncovers a subset associated with Alzheimer's disease. *Nat Commun* **11**, 6129, doi:10.1038/s41467-020-19737-2 (2020).
- 16 Young, A. P., Jackson, D. J. & Wyeth, R. C. A technical review and guide to RNA fluorescence *in situ* hybridization. *PeerJ* **8**, e8806, doi:10.7717/peerj.8806 (2020).
- 17 Im, K., Mareninov, S., Diaz, M. F. P. & Yong, W. H. An Introduction to Performing Immunofluorescence Staining. *Methods Mol Biol* **1897**, 299-311, doi:10.1007/978-1-4939-8935-5_26 (2019).
- 18 Cang, Z. & Nie, Q. Inferring spatial and signaling relationships between cells from single cell transcriptomic data. *Nat Commun* **11**, 2084, doi:10.1038/s41467-020-15968-5 (2020).
- 19 Asp, M., Bergensträhle, J. & Lundeberg, J. Spatially Resolved Transcriptomes-Next Generation Tools for Tissue Exploration. *Bioessays* **42**, e1900221, doi:10.1002/bies.201900221 (2020).
- 20 Marx, V. Method of the Year: spatially resolved transcriptomics. *Nat Methods* **18**, 9-14, doi:10.1038/s41592-020-01033-y (2021).
- 21 Ortiz, C., Carlén, M. & Meletis, K. Spatial Transcriptomics: Molecular Maps of the Mammalian Brain. *Annu Rev Neurosci* **44**, 547-562, doi:10.1146/annurev-neuro-100520-082639 (2021).
- 22 Scheltens, P. *et al.* Alzheimer's disease. *Lancet* **397**, 1577-1590, doi:10.1016/s0140-6736(20)32205-4 (2021).
- 23 Li, Q., Wu, X., Xu, L., Chen, K. & Yao, L. Classification of Alzheimer's Disease, Mild Cognitive Impairment, and Cognitively Unimpaired Individuals Using Multi-feature Kernel Discriminant Dictionary Learning. *Front Comput Neurosci* **11**, 117, doi:10.3389/fncom.2017.00117 (2017).
- 24 Silva, M. V. F. *et al.* Alzheimer's disease: risk factors and potentially protective measures. *J Biomed Sci* **26**, 33, doi:10.1186/s12929-019-0524-y (2019).
- 25 Vico Varela, E., Etter, G. & Williams, S. Excitatory-inhibitory imbalance in Alzheimer's disease and therapeutic significance. *Neurobiology of Disease* **127**, 605-615, doi:<https://doi.org/10.1016/j.nbd.2019.04.010> (2019).
- 26 Du, X., Wang, X. & Geng, M. Alzheimer's disease hypothesis and related therapies. *Translational Neurodegeneration* **7**, 2, doi:10.1186/s40035-018-0107-y (2018).
- 27 Leng, F. & Edison, P. Neuroinflammation and microglial activation in Alzheimer disease: where do we go from here? *Nat Rev Neurol* **17**, 157-172, doi:10.1038/s41582-020-00435-y (2021).
- 28 Edison, P., Donat, C. K. & Sastre, M. In vivo Imaging of Glial Activation in Alzheimer's Disease. *Frontiers in neurology* **9**, 625-625, doi:10.3389/fneur.2018.00625 (2018).
- 29 Wang, W.-Y., Tan, M.-S., Yu, J.-T. & Tan, L. Role of pro-inflammatory cytokines released from microglia in Alzheimer's disease. *Ann Transl Med* **3**, 136-136, doi:10.3978/j.issn.2305-5839.2015.03.49 (2015).
- 30 Bettcher, B. M., Tansey, M. G., Dorothée, G. & Heneka, M. T.

- Peripheral and central immune system crosstalk in Alzheimer disease - a research prospectus. *Nat Rev Neuro* **17**, 689-701, doi:10.1038/s41582-021-00549-x (2021).
- 31 Solár, P., Zamani, A., Kubíčková, L., Dubový, P. & Joukal, M. Choroid plexus and the blood-cerebrospinal fluid barrier in disease. *Fluids Barriers CNS* **17**, 35, doi:10.1186/s12987-020-00196-2 (2020).
- 32 Brioschi, S. *et al.* Heterogeneity of meningeal B cells reveals a lymphopoietic niche at the CNS borders. *Science* **373**, doi:10.1126/science.abf9277 (2021).
- 33 Cugurra, A. *et al.* Skull and vertebral bone marrow are myeloid cell reservoirs for the meninges and CNS parenchyma. *Science* **373**, doi:10.1126/science.abf7844 (2021).
- 34 Frieser, D. *et al.* Tissue-resident CD8(+) T cells drive compartmentalized and chronic autoimmune damage against CNS neurons. *Sci Transl Med* **14**, eabl6157, doi:10.1126/scitranslmed.abl6157 (2022).
- 35 Pappalardo, J. L. *et al.* Transcriptomic and clonal characterization of T cells in the human central nervous system. *Sci Immunol* **5**, doi:10.1126/sciimmunol.abb8786 (2020).
- 36 Pasciuto, E. *et al.* Microglia Require CD4 T Cells to Complete the Fetal-to-Adult Transition. *Cell* **182**, 625-640.e624, doi:10.1016/j.cell.2020.06.026 (2020).
- 37 Mittal, K. *et al.* CD4 T Cells Induce A Subset of MHCII-Expressing Microglia that Attenuates Alzheimer Pathology. *iScience* **16**, 298-311, doi:10.1016/j.isci.2019.05.039 (2019).
- 38 Camandola, S. & Mattson, M. P. Brain metabolism in health, aging, and neurodegeneration. *Embo j* **36**, 1474-1492, doi:10.15252/embj.201695810 (2017).
- 39 Baik, S. H. *et al.* A Breakdown in Metabolic Reprogramming Causes Microglia Dysfunction in Alzheimer's Disease. *Cell Metab* **30**, 493-507.e496, doi:10.1016/j.cmet.2019.06.005 (2019).
- 40 Choi, H. *et al.* Hippocampal glucose uptake as a surrogate of metabolic change of microglia in Alzheimer's disease. *J Neuroinflammation* **18**, 190, doi:10.1186/s12974-021-02244-6 (2021).
- 41 Xiang, X. *et al.* Microglial activation states drive glucose uptake and FDG-PET alterations in neurodegenerative diseases. *Sci Transl Med* **13**, eabe5640, doi:10.1126/scitranslmed.abe5640 (2021).
- 42 Sala Frigerio, C. *et al.* The Major Risk Factors for Alzheimer's Disease: Age, Sex, and Genes Modulate the Microglia Response to A β Plaques. *Cell Rep* **27**, 1293-1306.e1296, doi:10.1016/j.celrep.2019.03.099 (2019).
- 43 Deczkowska, A. *et al.* Disease-Associated Microglia: A Universal Immune Sensor of Neurodegeneration. *Cell* **173**, 1073-1081, doi:10.1016/j.cell.2018.05.003 (2018).
- 44 Keren-Shaul, H. *et al.* A Unique Microglia Type Associated with Restricting Development of Alzheimer's Disease. *Cell* **169**, 1276-1290.e1217, doi:10.1016/j.cell.2017.05.018 (2017).

- 45 Ellwanger, D. C. *et al.* Prior activation state shapes the microglia response to antihuman TREM2 in a mouse model of Alzheimer's disease. *Proc Natl Acad Sci U S A* **118**, doi:10.1073/pnas.2017742118 (2021).
- 46 Escartin, C. *et al.* Reactive astrocyte nomenclature, definitions, and future directions. *Nat Neurosci* **24**, 312-325, doi:10.1038/s41593-020-00783-4 (2021).
- 47 Liddelow, S. A. *et al.* Neurotoxic reactive astrocytes are induced by activated microglia. *Nature* **541**, 481-487, doi:10.1038/nature21029 (2017).
- 48 Habib, N. *et al.* Disease-associated astrocytes in Alzheimer's disease and aging. *Nature Neuroscience* **23**, 1-6, doi:10.1038/s41593-020-0624-8 (2020).
- 49 Fakhoury, M. Microglia and Astrocytes in Alzheimer's Disease: Implications for Therapy. *Curr Neuropharmacol* **16**, 508-518, doi:10.2174/1570159x15666170720095240 (2018).
- 50 Long, J. M. & Holtzman, D. M. Alzheimer Disease: An Update on Pathobiology and Treatment Strategies. *Cell* **179**, 312-339, doi:10.1016/j.cell.2019.09.001 (2019).
- 51 Mullard, A. Landmark Alzheimer's drug approval confounds research community. *Nature* **594**, 309-310, doi:10.1038/d41586-021-01546-2 (2021).
- 52 Song, C. *et al.* Immunotherapy for Alzheimer's disease: targeting β -amyloid and beyond. *Transl Neurodegener* **11**, 18, doi:10.1186/s40035-022-00292-3 (2022).
- 53 Gong, C. X., Liu, F. & Iqbal, K. Multifactorial Hypothesis and Multi-Targets for Alzheimer's Disease. *J Alzheimers Dis* **64**, S107-s117, doi:10.3233/jad-179921 (2018).
- 54 Zhang, F., Zhong, R. J., Cheng, C., Li, S. & Le, W. D. New therapeutics beyond amyloid- β and tau for the treatment of Alzheimer's disease. *Acta Pharmacol Sin* **42**, 1382-1389, doi:10.1038/s41401-020-00565-5 (2021).
- 55 Fu, W. Y., Wang, X. & Ip, N. Y. Targeting Neuroinflammation as a Therapeutic Strategy for Alzheimer's Disease: Mechanisms, Drug Candidates, and New Opportunities. *ACS Chem Neurosci* **10**, 872-879, doi:10.1021/acscchemneuro.8b00402 (2019).
- 56 Chen, W. T. *et al.* Spatial Transcriptomics and In Situ Sequencing to Study Alzheimer's Disease. *Cell* **182**, 976-991.e919, doi:10.1016/j.cell.2020.06.038 (2020).
- 57 Navarro, J. F. *et al.* Spatial Transcriptomics Reveals Genes Associated with Dysregulated Mitochondrial Functions and Stress Signaling in Alzheimer Disease. *iScience* **23**, 101556, doi:10.1016/j.isci.2020.101556 (2020).
- 58 Finak, G. *et al.* MAST: a flexible statistical framework for assessing transcriptional changes and characterizing heterogeneity in single-cell RNA sequencing data. *Genome Biol* **16**, 278, doi:10.1186/s13059-015-0844-5 (2015).

- 59 Yu, G., Wang, L. G., Han, Y. & He, Q. Y. clusterProfiler: an R package
for comparing biological themes among gene clusters. *Omics* **16**, 284-
287, doi:10.1089/omi.2011.0118 (2012).
- 60 Aevermann, B. *et al.* A machine learning method for the discovery of
minimum marker gene combinations for cell type identification from
single-cell RNA sequencing. *Genome Res* **31**, 1767-1780,
doi:10.1101/gr.275569.121 (2021).
- 61 Becht, E. *et al.* Dimensionality reduction for visualizing single-cell
data using UMAP. *Nat Biotechnol*, doi:10.1038/nbt.4314 (2018).
- 62 Oblak, A. L. *et al.* Comprehensive Evaluation of the 5XFAD Mouse
Model for Preclinical Testing Applications: A MODEL-AD Study.
Front Aging Neurosci **13**, 713726, doi:10.3389/fnagi.2021.713726
(2021).
- 63 Grubman, A. *et al.* Transcriptional signature in microglia associated
with A β plaque phagocytosis. *Nat Commun* **12**, 3015,
doi:10.1038/s41467-021-23111-1 (2021).
- 64 Chamling, X. *et al.* Single-cell transcriptomic reveals molecular
diversity and developmental heterogeneity of human stem cell-derived
oligodendrocyte lineage cells. *Nat Commun* **12**, 652,
doi:10.1038/s41467-021-20892-3 (2021).
- 65 Pan, J., Ma, N., Yu, B., Zhang, W. & Wan, J. Transcriptomic profiling
of microglia and astrocytes throughout aging. *J Neuroinflammation* **17**,
97, doi:10.1186/s12974-020-01774-9 (2020).
- 66 Sikora, E. *et al.* Cellular Senescence in Brain Aging. *Front Aging
Neurosci* **13**, 646924, doi:10.3389/fnagi.2021.646924 (2021).
- 67 Perry, V. H. & Gordon, S. Modulation of CD4 antigen on macrophages
and microglia in rat brain. *J Exp Med* **166**, 1138-1143,
doi:10.1084/jem.166.4.1138 (1987).
- 68 Nasrabady, S. E., Rizvi, B., Goldman, J. E. & Brickman, A. M. White
matter changes in Alzheimer's disease: a focus on myelin and
oligodendrocytes. *Acta Neuropathol Commun* **6**, 22,
doi:10.1186/s40478-018-0515-3 (2018).
- 69 Llorens, F., Gil, V. & del Río, J. A. Emerging functions of myelin-
associated proteins during development, neuronal plasticity, and
neurodegeneration. *Faseb j* **25**, 463-475, doi:10.1096/fj.10-162792
(2011).
- 70 Bettcher, B. M. *et al.* Astrogliosis and episodic memory in late life:
higher GFAP is related to worse memory and white matter
microstructure in healthy aging and Alzheimer's disease. *Neurobiol
Aging* **103**, 68-77, doi:10.1016/j.neurobiolaging.2021.02.012 (2021).
- 71 Schetters, S. T. T., Gomez-Nicola, D., Garcia-Vallejo, J. J. & Van
Kooyk, Y. Neuroinflammation: Microglia and T Cells Get Ready to
Tango. *Front Immunol* **8**, 1905, doi:10.3389/fimmu.2017.01905 (2017).
- 72 Safaiyan, S. *et al.* White matter aging drives microglial diversity.
Neuron **109**, 1100-1117.e1110, doi:10.1016/j.neuron.2021.01.027
(2021).
- 73 Polyzos, A. A. *et al.* Metabolic Reprogramming in Astrocytes

- Distinguishes Region-Specific Neuronal Susceptibility in Huntington Mice. *Cell Metab* **29**, 1258-1273.e1211, doi:10.1016/j.cmet.2019.03.004 (2019).
- 74 Song, Y.-H., Yoon, J. & Lee, S.-H. The role of neuropeptide somatostatin in the brain and its application in treating neurological disorders. *Experimental & Molecular Medicine* **53**, 328-338, doi:10.1038/s12276-021-00580-4 (2021).
- 75 Davies, P., Katzman, R. & Terry, R. D. Reduced somatostatin-like immunoreactivity in cerebral cortex from cases of Alzheimer disease and Alzheimer senile dementia. *Nature* **288**, 279-280, doi:10.1038/288279a0 (1980).
- 76 Iwata, N., Takaki, Y., Fukami, S., Tsubuki, S. & Saido, T. C. Region-specific reduction of A beta-degrading endopeptidase, neprilysin, in mouse hippocampus upon aging. *J Neurosci Res* **70**, 493-500, doi:10.1002/jnr.10390 (2002).
- 77 Jaramillo-Jimenez, A. *et al.* Association Between Amygdala Volume and Trajectories of Neuropsychiatric Symptoms in Alzheimer's Disease and Dementia With Lewy Bodies. *Frontiers in Neurology* **12**, doi:10.3389/fneur.2021.679984 (2021).
- 78 Poulin, S. P., Dautoff, R., Morris, J. C., Barrett, L. F. & Dickerson, B. C. Amygdala atrophy is prominent in early Alzheimer's disease and relates to symptom severity. *Psychiatry Res* **194**, 7-13, doi:10.1016/j.psychresns.2011.06.014 (2011).
- 79 Passaro, A. P., Lebos, A. L., Yao, Y. & Stice, S. L. Immune Response in Neurological Pathology: Emerging Role of Central and Peripheral Immune Crosstalk. *Front Immunol* **12**, 676621, doi:10.3389/fimmu.2021.676621 (2021).
- 80 Jadidi-Niaragh, F., Shegarfi, H., Naddafi, F. & Mirshafiey, A. The role of natural killer cells in Alzheimer's disease. *Scand J Immunol* **76**, 451-456, doi:10.1111/j.1365-3083.2012.02769.x (2012).
- 81 Solana, C., Tarazona, R. & Solana, R. Immunosenescence of Natural Killer Cells, Inflammation, and Alzheimer's Disease. *Int J Alzheimers Dis* **2018**, 3128758, doi:10.1155/2018/3128758 (2018).
- 82 Minjarez, B. *et al.* Identification of proteins that are differentially expressed in brains with Alzheimer's disease using iTRAQ labeling and tandem mass spectrometry. *J Proteomics* **139**, 103-121, doi:10.1016/j.jprot.2016.03.022 (2016).
- 83 He, Z. *et al.* Intraperitoneal injection of IFN- γ restores microglial autophagy, promotes amyloid- β clearance and improves cognition in APP/PS1 mice. *Cell Death Dis* **11**, 440, doi:10.1038/s41419-020-2644-4 (2020).
- 84 Potter, H. *et al.* Safety and efficacy of sargramostim (GM-CSF) in the treatment of Alzheimer's disease. *Alzheimer's & Dementia: Translational Research & Clinical Interventions* **7**, e12158, doi:<https://doi.org/10.1002/trc2.12158> (2021).
- 85 Machhi, J. *et al.* CD4+ effector T cells accelerate Alzheimer's disease in mice. *J Neuroinflammation* **18**, 272, doi:10.1186/s12974-021-

- 02308-7 (2021).
- 86 Saresella, M. *et al.* Increased activity of Th-17 and Th-9 lymphocytes and a skewing of the post-thymic differentiation pathway are seen in Alzheimer's disease. *Brain Behav Immun* **25**, 539-547, doi:10.1016/j.bbi.2010.12.004 (2011).
- 87 Kalluri, R. & LeBleu, V. S. The biology, function, and biomedical applications of exosomes. *Science* **367**, doi:10.1126/science.aau6977 (2020).
- 88 Harting, M. T. *et al.* Inflammation-Stimulated Mesenchymal Stromal Cell-Derived Extracellular Vesicles Attenuate Inflammation. *Stem Cells* **36**, 79-90, doi:10.1002/stem.2730 (2018).
- 89 Sarker, A. *et al.* [64Cu]Cu-Albumin Clearance Imaging to Evaluate Lymphatic Efflux of Cerebrospinal Space Fluid in Mouse Model. *Nuclear Medicine and Molecular Imaging*, doi:10.1007/s13139-022-00746-6 (2022).

국문 초록

알츠하이머병 모델에서 공간 전사체

시그니처 및 치료 작용 원리 규명

이은지

분자의학 및 바이오제약학과

서울대학교 대학원

알츠하이머병 진행에 따른 병태생리학적 변화는 다양한 연구를 통해 비교적 잘 검증되었지만 뇌의 공간적 이질성에 대한 이해를 기반으로 한 연구가 여전히 필요하다. 또한 다인성 질환인 알츠하이머병에 대한 치료 효과를 종합적으로 검증하기 위한 방법이 제한적이다. 최근, 공간 전사체 데이터를 통한 개별 뇌 영역에서의 주요 유전자 및 관련 기능에 대한 식별이 가능해졌다. 본 연구에서는 뇌 영역별 전체 유전자 발현 및 세포 유형 변화를 동시에 검출할 수 있는 공간 전사체 분석방법을 기반으로 알츠하이머병의 병리학적 변화를 연구하고 치료 효과를 평가하고자 하였다.

첫 번째로, 공간 전사체학을 기반으로 인지 장애 발생 전과 후의 알츠하이머병 모델을 분석하였다. 알츠하이머병 병리 초기의 백질에서 신경교세포의 활성화가 확인되었다. 병리의 진행에 따라 신경 교세포 활성 관련 유전자들은 백질과 회색질 모두에서 전체적으로 상향 조절되는 경향을 보였다. 반면, 하향 조절되는 유전자 관련 기능은 지역 별로 상이함을 확인하였다. 그에 더하여 선별된 유전자 조합을 사용하여 다양한 뇌세포의 공간 분포를 조사하였다. 백질에서 활성 미세아교세포와 성상 교세포 관련 유전자들의 초기 변화를 확인하였으며, 이는 결국 병리 진행에 따라 회색질로 퍼짐이 확인되었다. 추가적으로, 신경 세포, 대사, 노화, 및 항원 제시 관련 유전자에 대한 변화 분포가 조사되었다.

다음으로, 알츠하이머병 모델에서 Y 형 미로 행동 분석을 통해 NK 세포 투여 및 항 CD4 항체에 대한 인지 기능 향상 효과를 확인하였다. NK 세포 치료는 뇌 전반에 걸쳐 신경 교세포 관련 유전자의 감소와 세포 호흡 관련 유전자의 증가를 보였다. 변화되는 세포 시그니처로는 활성 미세아교세포의 회색질에서의 감소와 억제성 신경 세포의 편도체에서의 지역 특이적 감소가 확인되었다. 반면, 항 CD4 항체 주입은 백질에서 지역 특이적으로 시냅스 기능 관련 유전자의 증가가 확인되었지만 효과가 미미했으며 주요 뇌 세포 시그니처의 변화도 유의하게 확인되지 않았다.

종합해 보면, 위 결과를 통해 알츠하이머병의 병리 진행에 따른 뇌 각 영역별 유전자 발현 및 뇌세포 시그니처의 시공각적 변화를 확인할 수 있었다. 두가지 약물 투여를 예로 들어 알츠하이머병 모델에서의 효과를 검증하는 방법으로 공간전사체 분석의 적용 가능성은 보여주었다. 상기 확립된 공간전사체 분석방법을 통해 다양한 질병에 적용하여 더욱 정확하고 종합적으로 질환의 진행 정도 및 치료제에 대한 효능/기전을 검증하는 데 활용될 것으로 기대하고 있다.

Keywords: 공간 전사체; 뇌 공간적 이질성; 알츠하이머병;

신경교세포 활성; 면역 조절

Student Number: 2018-35220